Varying growth behavior of redox-sensitive nanoparticles on 1:1 and 2:1 clay surfaces: Mechanistic insights on preferential toxic ions removal in mono, co, and multi-metal contaminated waters

Nitin Khandelwal [a,b], Nisha Singh [a,c], Ekta Tiwari [a,d], Rémi Marsac [e], Dieter Schild [f], Thorsten Schäfer [g], Gopala Krishna Darbha [a,h,*]

[a] Environmental Nanoscience Laboratory, Department of Earth Sciences, Indian Institute of Science Education and Research (IISER) Kolkata, Mohanpur, West Bengal 741246, India
[b] Environmental Engineering Laboratory, Department of Civil Engineering, McGill University, Montreal H3A 0C3, Quebec, Canada
[c] Japan Agency for Marine-Earth Science and Technology (JAMSTEC), 2-15 Natsushima, Yokosuka, Kanagawa 237-0061, Japan
[d] Natural Resources Management & Environmental Sciences, College of Agriculture, Food & Environmental Sciences, California Polytechnic State University, CA 93401, USA
[e] Univ Rennes, CNRS, Géosciences Rennes - UMR 6118, F-35000 Rennes, France
[f] Karlsruhe Institute of Technology (KIT), Institute for Nuclear Waste Disposal, Hermann-von-Helmholtz-Platz 1, 76344 Eggenstein-Leopoldshafen, Germany
[g] Institute of Geosciences, Applied Geology, Friedrich-Schiller-University Jena, Burgweg 11, D-07749 Jena, Germany
[h] Centre for Climate and Environmental Studies, Indian Institute of Science Education and Research (IISER) Kolkata, Mohanpur, West Bengal 741246, India

ARTICLE INFO

Keywords:
nZVI
Sorption
Kaolinite
Bentonite
Metals removal
Reductive co-precipitation

ABSTRACT

In the current study, contrasting growth behaviour of redox sensitive Fe^0 nanoparticles (nZVI) was observed on different clay surfaces i.e., 1:1 non-swelling kaolinite (K-nZVI) and 2:1 swelling bentonite (B-nZVI). Osmotic swelling of bentonite led to Fe^0 nucleation and growth of 5–7 nm size particles in the broadened interlayer spaces. B-nZVI had negative zeta potential due to the domination of the surface charge of bentonite clay. In contrast, kaolinite has shown dominant surface growth of nZVI particles (>24.8 ± 7.4 nm) and positive zeta potential, suggesting domination of Fe^0 nanoparticles (nZVI) characteristics. This surface-dependent variation led to higher and faster removal of oxy-anions with K-nZVI, i.e., chromium and arsenic (87.5 and 157.35 mg/g) than B-nZVI (18.4 and 86.9 mg/g). In comparison, B-nZVI has shown higher sorption of cations i.e., nickel and cadmium (36 mg/g and 46 mg/g) than K-nZVI (25 and 27 mg/g). XPS and pXRD analysis of reaction precipitates confirmed reductive sorption of chromium, co-precipitation/ complexation of arsenic, electrostatic attraction and complexation of nickel and cadmium as major removal mechanisms. Drastically higher total contaminant sorption capacities of B-nZVI (327 mg/g) and K-nZVI (372 mg/g) in multi-contaminant (Cr + As + Ni + Cd) solutions than individual capacities in mono-ionic solutions was due to co-operative effects and newer sites induced *via* sorption and redox-transformation of other ionic species. K-nZVI removed chromium and arsenic to below drinking water permissible limits whereas B-nZVI succeeded in separating nickel and cadmium to drinkable levels in groundwater, freshwater, river water, and wastewater samples, emphasizing their applicability in high cationic—low anionic and low cationic-higher anionic species contaminated waters, respectively.

1. Introduction

Water is a unique entity of the planet and one of the most critical resources required for balanced ecosystem functioning. According to recent estimates, three out of every ten people do not have access to contamination-free drinking water [1]. Tremendously increasing water use by nearly 1% per year has resulted in having 3.6 billion people or 47%, of total world population suffering with water scarcity at least one month every year [2]. In an extensive range of contaminants, increasing concentrations of heavy metals and metalloids in water bodies represent an alarming environmental threat because of their non-degradability and environmental persistence [3]. Once introduced in the

* Corresponding author at: Centre for Climate and Environmental Studies, Indian Institute of Science Education and Research (IISER) Kolkata, Mohanpur, West Bengal 741246, India.
E-mail addresses: gkdarbha@gmail.com, gkdarbha80@yahoo.com (G. Krishna Darbha).

environment, these ions tend to bioaccumulate, impact the whole food chain and ultimately threaten human health [4,5]. In a prevailing environmental condition, these ions can speciate in various ionic species [6]. For example- as shown in fig. S1 a-d, in circum-neutral pH conditions and oxidizing environment, arsenic (As) and chromium (Cr) speciates in anionic species, i.e., arsenate and chromate ions [7,8], whereas nickel (Ni) and cadmium (Cd) stay in their cationic +2 form [9].

This variation in ionic behavior requires selectivity or a component additive approach as a critical component in the remediation technique [10]. Moreover, the co-contamination of ions with similar charge behavior can induce site competition in the system and may make the remediation even more challenging. Similarly, solutions contaminated with multiple ions of varying charge can also impact the treatment efficiency [11]. Several explored removal techniques include conventional methods that suffer from limited selectivity and sorption capacity, such as filtration, sedimentation, coagulation-flocculation, aerobic and anaerobic degradation, etc. [12]. Bioremediation, including phytoremediation, suffers from slower reaction kinetics [13]. Other remediation techniques are distillation, solvent extraction, microfiltration, ultrafiltration, reverse and forward osmosis, electrolysis, etc., with high power consumption and tedious setup and maintenance [14]. Sorption-assisted water treatment techniques involve cost-effectiveness, environmentally friendly nature, high selectivity and removal capacity, process simplicity, no secondary contamination, and low power consumption, etc., and are therefore of prime interest to the scientific community [15]. Redox-sensitive nano-adsorbents, such as magnetic nanoparticles, Fe_3O_4, graphene, etc., have recently emerged and been explored for their added electron transferring ability at the surface-water interface [16,17]. It can lead to simultaneous redox transformation of toxic metals, forming co-precipitate with insoluble metal oxy-hydroxides on the nanocomposite surface [18,19].

Instant inert surface oxide shell formation and self-aggregation of these redox-sensitive nanoparticles in the natural environment generally limits their applicability [20]. Research showed that supporting surfaces, such as clays, graphene, biochar, charcoal, etc., can preserve their redox state [16,21]. Clays dominate out of several supporting surfaces because of their natural abundance, eco-friendly nature, and high cation exchange capacity that can prevent secondary contamination [22]. Clays are hydrous alumino-silicates and have a flake-like structure. Based on the crystal structure, i.e., a combination of tetrahedral (T) and octahedral (O) layers, kaolinite (1:1- T:O type), and bentonite containing around 80% of montmorillonite (2:1- *T*-O-T type) are two major clays [23]. Both kaolinite and bentonite have been explored to support redox-sensitive nanoscale zerovalent iron (nZVI) [24,26]. Despite a drastic variation in the crystal structure and material properties, i.e., kaolinite with non-swelling nature and less interlayer spacing leading to limited cation exchange capacity (CEC), while bentonite having swelling (>10 times) nature, and very high CEC, etc., surface-associated variations in growth behavior of redox-sensitive nanoparticles and its impact on contaminant sorption behavior are still unknown.

Recently researchers have synthesized different clay-nZVI nanocomposites for the removal of various contaminants. For example, Baldermann et al. supported NANOFER 25 nZVI suspension on bentonite clay and used it to remove trichloroethylene (TCE), where nanoparticles were attached only on the surface [27]. Shi et al. showed B-nZVI formed using a liquid-phase reduction technique had around 18.7 mg/g of CrO_4^{2-} sorption capacity [24]. Whereas, Üzüm et al. [25] found that kaolinite-supported nZVI can remove Cu^{2+} and Co^{2+} ions with 140 mg/g and 25 mg/g of sorption capacity. Reductive co-precipitation of contaminants was due to electron transfer from Fe^0 and its oxidation to oxy-hydroxides [28]. So far, clays are only considered a supporting material to prevent Fe^0 nanoparticle agglomeration and preserve their reactivity [22].

However, dominating role of variation in crystal structure and properties of clays in deciding or controlling the sorption behavior of nZVI nanocomposites for various ionic contaminants is unknown. Here, based on the variations in crystal structures of different clays, we hypothesized that 1:1 clay having limited or no interlayer spacing and non-swelling nature could result in the growth of nZVI mostly on the surface. In contrast, swelling is widespread in 2:1 montmorillonite clay due to hydration [29]. It is reported that Na- bentonite can show two different swellings, i.e., crystalline swelling (limited d-spacing increase) and osmotic swelling resulting in a larger d-spacing increase (even > 50 Å) [30]. Osmotic swelling happens at a lower salt concentration (<0.5 M) of monovalent ions [30]. Therefore, supporting nZVI on swelling 2:1 bentonite clay can lead to the growth of nanoparticles in inter-layer spaces. The variation in the growth behavior of Fe^0 nanoparticles on different clay surfaces can further alter the surface properties such as nanoparticles size, charge, and surface area, etc., leading to varying sorption behavior for ionic contaminants.

To test the hypothesis, B-nZVI and K-nZVI nanocomposites were synthesized and sorption behavior was tested in mono, co, and multi-contaminant systems by utilizing different contaminants, i.e., oxyanions (chromium, arsenic), and metal cations (nickel, cadmium). Detailed batch sorption studies and surface characterization using dynamic light scattering (DLS), powder X-ray diffraction (pXRD), Fourier-transform infrared (FTIR) spectroscopy, and X-ray photoelectron spectroscopy (XPS) were done to delineate preferential sorption of contaminants and associated removal mechanisms of nanocomposites.

2. Materials and methods

2.1. Materials and chemicals

Clays used include- extra pure Na-bentonite (Loba Chemie Pvt. ltd., India) with composition (wt%)- 54.9% SiO_2, 19.2% Al_2O_3, 8.3% Fe_2O_3, 3.79% Na_2O, 1.99% MgO, 1% K_2O and 0.17% CaO [21], and kaolinite (Charco Chemicals, India) with composition- 55.51% SiO_2, 28.6% Al_2O_3, 0.6% Fe_2O_3, 0.1% Na_2O, 0.02% MgO, 4.55% K_2O and 0.06% CaO. Chemicals purchased from Merck, Germany, are Ethanol, $NaAsO_2$ 0.05 N solution, $Ni(NO_3)_2{\cdot}6H_2O$, and $FeCl_3{\cdot}6H_2O$. Merck, India supplied $CdCl_2.H_2O$, $K_2Cr_2O_7$, HNO_3, NaOH, $NaBH_4$, and $NaNO_3$. 18.2 MΩ.cm Milli-Q water was used for preparing all solutions.

2.2. Synthesis of nanocomposites

To synthesize bentonite and kaolinite supported nZVI nanocomposites (B-nZVI and K-nZVI, respectively), clay, and iron salt with a 1:1 mass ratio were introduced to 4:1 ethanol: water interfacial solution [16]. The suspension was sonicated for 30 min, followed by vigorous stirring. Then $NaBH_4$ (1 M) was added dropwise at a flow rate of 4.5 mL/min to the suspension under constant stirring.

The reaction mixture was left for another 20 min on vigorous stirring after $NaBH_4$ addition to ensure complete reduction. Then the obtained precipitate was filtered, washed multiple times with ethanol and water, and vacuum dried.

2.3. Characterization of nanocomposites

Clay surface morphology was visualized using field emission scanning electron microscopy (FESEM, Carl Zeiss SUPRA 55VP), and size distribution was obtained using particle size analyzer (ZEN3600, Malvern, UK), whereas synthesized nanocomposites were analyzed using FESEM and ultra-high-resolution transmission electron microscopy, i.e., UHR-FEG-TEM (JEOL, JEM 2100F). Elemental composition, mapping, and line scans were obtained using EDAX analysis through INCA software (Oxford Instruments, X-Max) coupled with UHR-FEG-TEM. Specific surface area and pore size distribution using Micromeritics Gemini VII BET-N_2 surface area analyzer. The nitrogen adsorption/desorption isotherms are reported by BJH (Barrett Joyner-Halenda) surface analysis method. Before analysis, samples were degassed in vacuum at 150 °C for 12 h. Crystallinity and phase characteristics were obtained by powder X-ray diffraction (pXRD) of materials. pXRD measurements were taken

using benchtop powder X-ray diffractometer (Rigaku mini flex) having Cu Kα 1.54059 Å radiation at 40 kV/15 mA. Samples were scanned in the range of 5^0-65^0 2θ at 5^0 per minute and step size of 0.02^0. Surface functionality was interpreted using Fourier transform infrared spectroscopy (FTIR) by analyzing KBr pellets using Thermo-Scientific Nicolet iS5 coupled with the iD1 transmission accessory. Zeta Sizer (ZS-90, Malvern) coupled with MPT-2 pH auto-titrator was used to obtain zeta potential and point of zero charges (pH_{PZC}) of nanocomposites. Reaction precipitates were also analyzed using a PHI 5000 VersaProbe II (ULVAC-PHI Inc.) equipped with a monochromatic Al Kα X-ray source (1486.7 eV) for XPS measurements. Elemental lines are charge referenced to C1s (C_xH_y) at 284.8 eV.

2.4. Batch sorption experiments and analytical techniques

At pH 6.5, 0.01 M $NaNO_3$ solutions were introduced with (i) mono contaminant system, i.e., arsenic, chromium, nickel, and cadmium individually, (ii) co-contaminant systems, i.e., anionic (An), i.e., arsenic-chromium and cationic (Ct), i.e., nickel–cadmium and (iii) multi-contaminant systems (MM), i.e., arsenic-chromium-nickel–cadmium. With a fixed weight of adsorbent, i.e., 20 mg, and a solution volume of 25 mL, sorption kinetics was performed at 20 mg/L concentrations of respective contaminants by varying the interaction time. At the same time, sorption isotherm experiments were performed by varying contaminant concentrations in 10–60 mg/L range by keeping interaction time constant to 12 h, which is more than the obtained equilibrium time. Reaction mixtures were kept on shaking (200 RPM) at 25 ^{0}C. After the interaction, mixtures were centrifuged, and reaction precipitates were dried for further characterization. Supernatants were filtered using 0.22 μm filter paper, acidified, and analyzed for respective contaminant concentrations using ICP-OES (Thermo iCAP-7400 series). Samples were also analyzed for released iron concentration after the interaction to ensure minimal secondary contamination. Sorption behavior was also evaluated (i) as a function of pH and (ii) in different types of water compositions, i.e., synthetic freshwater, groundwater, wastewater, and natural river water (compositions provided in table- S1a-b in supplementary information), to ensure environmental applicability of nanocomposites. For that, 20 mg of adsorbent was taken in 25 mL of the solution with having 10 mg/L concentration of each metal ion. All the experiments were performed in duplicates, and errors are shown wherever significant (>5%). Performed blanks include (i) all stated combinations of contaminated solutions without adding adsorbents and (ii) solutions containing nanocomposites without adding contaminants.

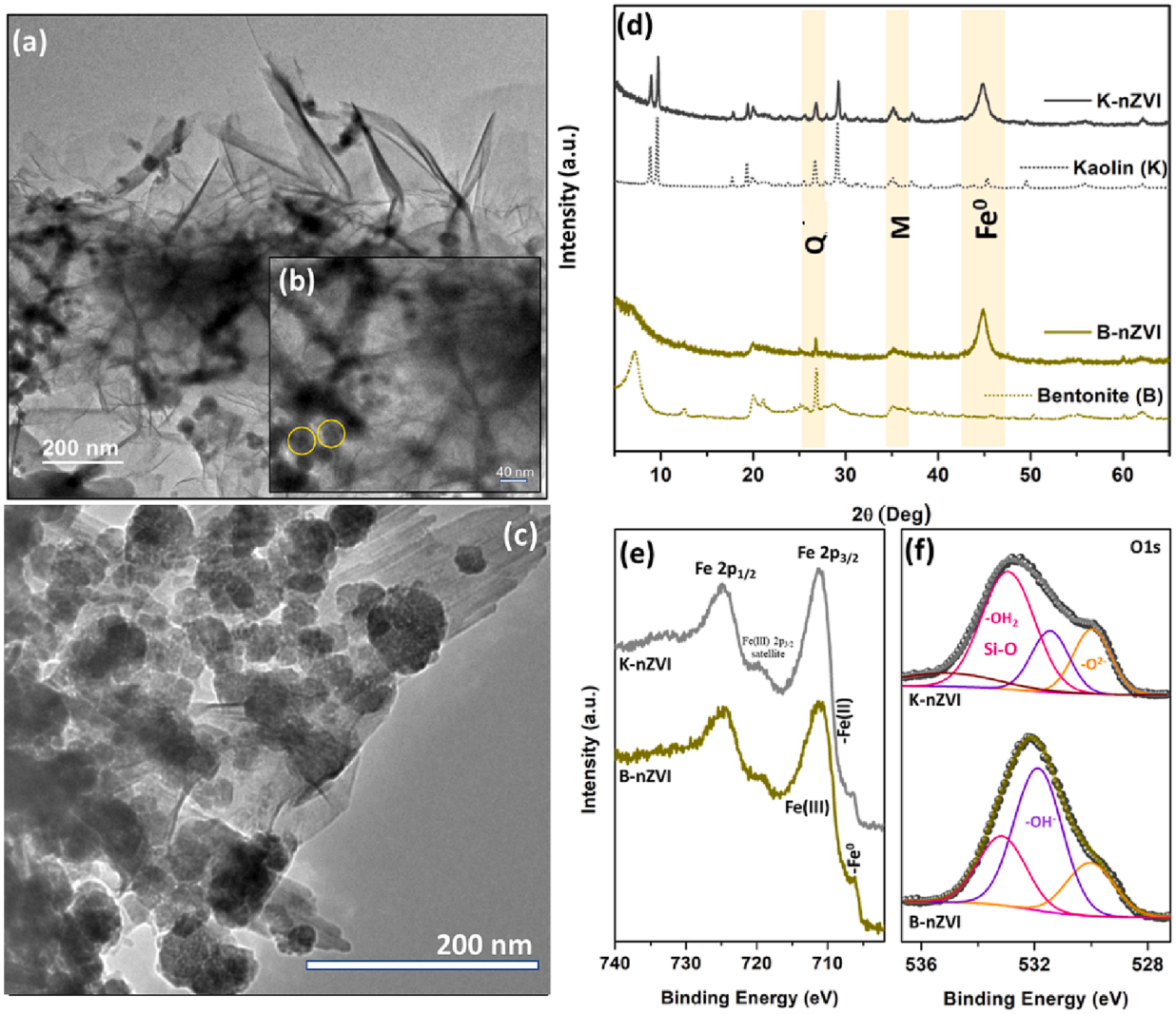

Fig. 1. TEM images of (a) and inset (b) B-nZVI, (c) K-nZVI, (d) pXRD spectra of clay and nZVI nanocomposites [Q = quartz, M = magnetite] and XPS spectra of B-nZVI and K-nZVI for (e) Fe2p and (f) O1s regions.

3. Results and discussion

3.1. Surface characteristics and particles growth behavior

3.1.1. Morphology, composition, and growth mechanisms

The sheet-like structure of both bentonite and kaolinite can be visualized through SEM images in Fig. S2a, and S3a. FESEM images showed that most of the clay flakes were of size < 2 μm while obtained hydrodynamic diameter using particle size analyzer (Fig. S2b, and S3b), showed a size distribution up to 100 μm with most particles < 10 μm. This increased size corresponds to aggregates formed in suspension. After nZVI growth, clay surfaces show the presence of spherical nanoparticles, as observed in HRTEM images in Fig. 1 a-c. FESEM images of B-nZVI (Fig. S2 c-d) showed a clear variation having bright interlayer cross-sections compared to K-nZVI where Fe^0 nanospheres were clearly visible only attached on the surface (Fig. S3 c-d).

Particles size distribution analysis using multiple TEM images (Fig. 1 a-c, Fig. S2 e-f, and Fig. S3 e-f) showed two distinct size distributions of Fe^0 nanoparticles in B-nZVI, i.e., 5.8 ± 2.6 nm and 20.6 ± 8.7 nm corresponding to growth of particles in interlayers and surface of bentonite, respectively. In contrast, iron nanoparticles covered the surface of kaolinite with a diameter of 24.8 ± 7.4 nm. Elemental mapping in Fig. S4 a, b showed the enhanced intensity of iron signal over spherical particles and the presence of oxygen and silicon in the background supporting the growth of iron nanoparticles on clay surfaces. Fig. 1d shows the pXRD pattern of clays and synthesized nanocomposites. The characteristic d-001 peak of bentonite around 2θ 7.14^0 corresponding to an interlayer spacing of 1.27 nm [31] shifted and broadened after iron loading, suggesting the broadening of interlayer space which can be attributed to Fe^0 nucleation and growth in interlayers. Earlier, Son et al. have also observed a peak shift of d001 in bentonite after iron-oxide loading due to formation of polycations and particles in the interlayers [32]. In K-nZVI, the d-001 peak of kaolinite around 2θ 12^0 was present with no shifting or broadening, supporting no significant change in the interlayer spacing [33]. Simultaneously, the generation of characteristic Fe^0 peak near 2θ 44.8^0, along with the absence of iron oxide peaks [34,35], suggests that iron particles were in preserved redox state on both clay surfaces with no dominant crystalline iron-oxide phases or thick oxide shells.

The surface of nanocomposites was further evaluated using XPS spectra and by fitting Fe2p and O1s regions (Fig. 1 e-f). Obtained peaks around 706.9 eV, 711.1 eV, 724.9 eV, and 719.9 eV of binding energies corresponded to Fe(0) $2p_{3/2}$, Fe(III) $2p_{3/2}$, Fe(III) $2p_{1/2}$ and satellite peak of Fe(III) $2p_{3/2}$. Fitting reveals the presence of Fe(II) and Fe(III) along with Fe^0 on the surface in both kaolinite and bentonite [36]. It can be attributed to a very thin shell of iron-oxy—hydroxides on the surface of elemental iron nanoparticles. Higher Fe^0 content on bentonite surface compared to kaolinite can be attributed to nanoparticles coverage with bentonite flakes as observed in TEM images.

In summary, two distinct size fractions of nZVI in bentonite, broadening of interlayer spacing as obtained from pXRD, and higher Fe^0 content in B-nZVI compared to no change in d001 peak of kaolinite after nZVI growth, and > 20 nm particles attached on the surface, suggest the following, iron nanoparticles growth mechanisms (Scheme 1): initially, the addition of bentonite in ethanol:water interfacial solution can result in its crystalline swelling, which allows iron ions to enter and adsorb in the inter-layer spaces and on the surface as well. Once the addition of $NaBH_4$ begins, iron particles start to nucleate, and simultaneously interlayer spacing of bentonite clay increases due to its osmotic swelling [37,38]. It may easily allow iron nanoparticles to grow in the interlayer spaces and on the surface. On the other hand, kaolinite is 1:1 clay and does not swell, which results in the surface sorption and growth of iron nanoparticles [26].

3.1.2. Surface area and pore distribution

BET-N_2 adsorption–desorption isotherms are shown in Fig. S5 a, c. Pertaining to limited inter-layer space, kaolinite clay showed a BET-N_2 surface area of 3.15 m^2/g, whereas it was 24.5 m^2/g for bentonite [39,40]. Literature reports show that bare nZVI particles have a surface area of around 20–25 m^2/g [41,42]. After nZVI growth, bentonite surface area increased further to 31.1 m^2/g, corresponding to the growth of very small (5–7 nm) iron nanoparticles. In contrast, K-nZVI showed a surface area of 19.4 m^2/g which was higher than kaolinite but was in range with the surface area of bare nZVI particles [25,43]. A decrease in the pores (≈ 4 nm) having a maximum volume in B-nZVI compared to bentonite suggests nZVI growth in available pores (Fig. S5b). While an increase in the pore volume (Fig. S5d) in K-nZVI can be attributed to nanoscale particles growth on the surface. These observations further support the proposed Fe^0 particles growth mechanisms on different clay surfaces. Further details of obtained surface area, average pore diameter, and cumulative pore volume are provided in Table S2. B-nZVI has shown a slightly higher cumulative pore volume than bentonite, which may be due to the growth of some nZVI particles on the clay surface.

3.1.3. Surface functionality and charge

Both kaolinite and bentonite shared almost similar surface functionality. FT-IR spectra (Fig. S5e) showed a broad peak around 3430 cm^{-1} for –OH group stretching. 1044 cm^{-1} peak was due to Si-O bending vibration, while antisymmetric Si-O-Si stretching vibration caused an adsorption peak near 797 cm^{-1} [44]. Kaolinite group minerals show –OH bands at 3696, 3669 and 3651 cm^{-1} beside the 3619 cm^{-1} inner hydroxyl group band while 1632 cm^{-1} peak of O—H reflected crystal water in clays lattice [45]. A shift in the 1632 cm^{-1} O—H peak and the generation of an adsorption band at 670 cm^{-1} was due to the

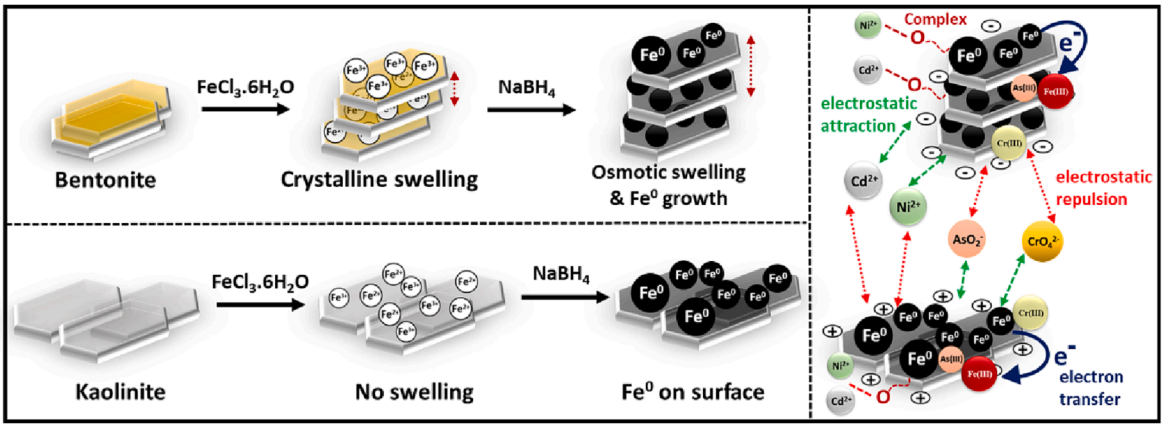

Scheme 1. Synthesis and growth mechanisms of nZVI on bentonite and kaolinite surfaces and respective contaminant removal mechanisms.

symmetric Fe-O stretch of goethite (α-FeOOH)[46].

This variation in the growth behavior of nZVI particles, i.e., the domination of bentonite in B-nZVI and of nZVI in K-nZVI, can also be correlated with variation in the zeta potentials of various nanocomposites (Fig. 2a). The negative zeta potential of both the clays, i.e., < 30 mV, can be attributed to isomorphic substitution in their crystal structures [47]. It decreased but remained negative even after nZVI growth in the case of B-nZVI, confirming bentonite domination. Whereas, after nZVI growth, K-nZVI shows the point of zero-charge at pH 8 i.e., at pH < 8 K-nZVI has positive zeta potential. The positive zeta potential can be attributed to partial oxidation of nZVI particles and protonation of surface oxide layer. Therefore, in the environmentally relevant pH conditions (pH 6–8) B-nZVI holds a negative charge, whereas K-nZVI was dominantly positive. This variation resulted from the drastic difference in nZVI growth behavior on both surfaces and is crucial for the adsorbent's selectivity towards specific toxic ions, as observed in later sections.

3.2. Contaminant sorption behavior and mechanisms

Preliminary sorption experiments with raw constituents of the nanocomposites i.e., bentonite and kaolinite clays and bare nZVI particles, were performed for all the studied contaminants and compared for respective sorption capacities with the synthesized nanocomposites. Results in Fig. 2b show minimal sorption of oxy-anions (<2.5 mg/g) with both clays. Bare nZVI show significant sorption of oxy-anions but limited sorption of cationic species (<5.5 mg/g). In comparison, synthesized nanocomposites showed higher removal of both cations (>18 mg/g) and oxy-anions (>13.5 mg/g). In all the cases, iron release from bare nZVI particles was higher than the WHO-defined permissible limit of 2 mg/L for drinking water. Whereas no significant iron release was observed in the case of nanocomposites. Results confirm that nanocomposites advance their raw constituents regarding contaminant sorption capacities and prevent the secondary release of pollutants. Interestingly, both B-nZVI and K-nZVI showed a drastic variation in contaminant-specific sorption capacities. At a fixed concentration of toxic anions and cations, B-nZVI showed comparatively higher removal of nickel and cadmium, whereas K-nZVI separated chromium and arsenic with high efficiency (Fig. 2b). This variation in sorption capacities might be directly correlated with the positive and negative zeta potentials of K-nZVI and B-nZVI (Fig. 2a), respectively, allowing faster interaction and bulk transfer of oppositely charged ions on the surface.

After the sorption of toxic ions, reaction precipitates were collected and thoroughly characterized for change in surface charge, crystallinity, functionality, and redox composition to delineate various involved removal mechanisms. Interaction and removal mechanisms were found to be varying for different contaminants for B-nZVI and K-nZVI and are described below in detail.

3.2.1. Chromium

Chromium which speciate in the form of CrO_4^{2-} oxy-anions, had varying interaction with B—nZVI and K-nZVI. Zeta potential (Fig. 3 a-b) of B-nZVI in 0.01 M $NaNO_3$ solution was 16.7 ± 1.3 mV which decreased to 13.3 ± 0.4 mV after interaction with chromate ions. The sole involvement of electrostatic attraction should have resulted in either increased negative zeta potential or electrostatic repulsion with chromate ions, suggesting the involvement of other removal mechanisms. Similarly, zeta potential of K-nZVI was + 12.1 ± 0.7 mV which decreased to + 8.5 ± 1.3 mV after interaction with chromate ions supporting the involvement of electrostatic attraction. But, a slight decrease in zeta potential points out the presence of different species of chromium on K-nZVI surface as well. These observations were further supported by pXRD spectra (Fig. 3c-d), which showed a slight decrease in the intensity of Fe^0 peak in B-nZVI and little oxidation of iron on B-nZVI surface, suggesting limited electron transfer and redox-transformation in the system leading to limited interaction of B—nZVI with chromium. K-nZVI showed a drastic decrease in 44.8^0 Fe^0 peak and generation of 30^0 and 35^0 intense iron-oxide peaks suggesting intense electron transfer and iron oxidation. FTIR spectra (Fig. 3 e-f) also showed the enhanced intensity of 530 cm^{-1} Fe-O stretching. Redox transformation of chromium and nanocomposites was further confirmed by obtaining XPS survey scans (Fig. S6a-b) and high-resolution scans for Fe2p (Fig. S6c—d), O1s (Fig. 4a) and Cr2p regions (Fig. 4f). Fe^0 associated peak near 707 eV disappeared after interaction with chromium in both B—nZVI and K-nZVI confirming electron transfer and consumption of Fe^0. In correspondence, Fe(II) and Fe(III) contribution increased on the surface.

Cr2p spectra showed a dominant presence (72.8% and 79.6%) of Cr (III) near 577 eV on B-nZVI and K-nZVI surfaces, confirming the reduction of chromium on both surfaces [48,49]. K-nZVI showed higher intensity of Cr2p-associated peaks compared to B-nZVI. O1s spectra showed the dominance of $–OH^-$ functional groups in B-nZVI and both $–OH^-$ and $–O^{2-}$ groups in K-nZVI (Fig. 4a) after interaction with chromium, suggesting the simultaneous formation of iron oxides/oxy-hydroxides and chromium oxide/oxy-hydroxide. In combination, zeta potential, pXRD, and XPS data confirm strong interaction and higher redox-transformation of chromate ions with K-nZVI and co-precipitation with formed iron-oxy-hydroxides compared to B-nZVI, which was also supported by experimental sorption capacities data provided in later

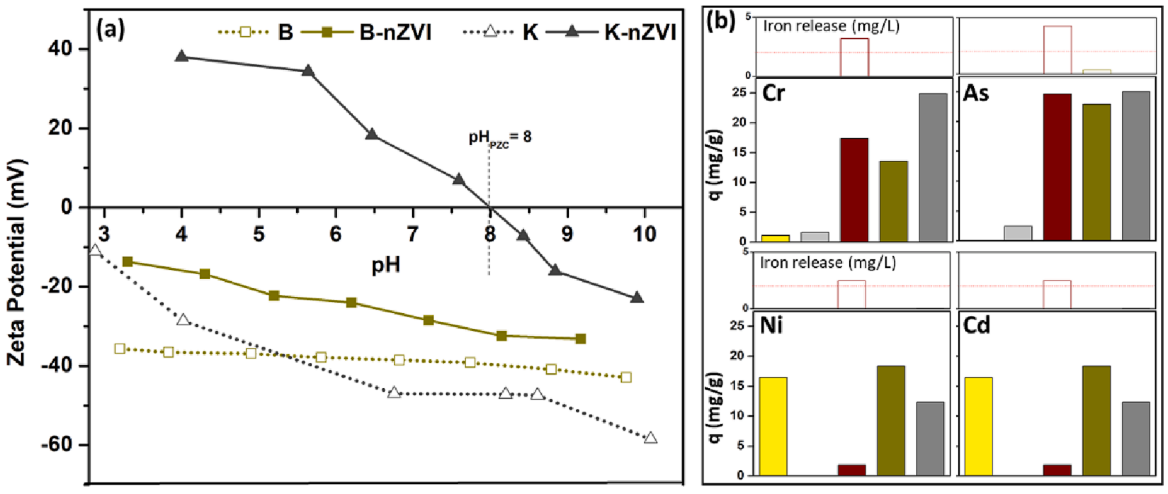

Fig. 2. (a) Zeta potential at varying pH for clays and synthesized nanocomposites and (b) Sorption capacity of raw constituents of nanocomposites i.e., Bentonite, Kaolinite and nZVI and synthesized nanocomposites i.e., B-nZVI and K-nZVI [m = 20 mg, V = 20 mL, C_0 = 20 mg/L, T = 25 °C, RPM = 200, pH = 6.5, t = 12 h].

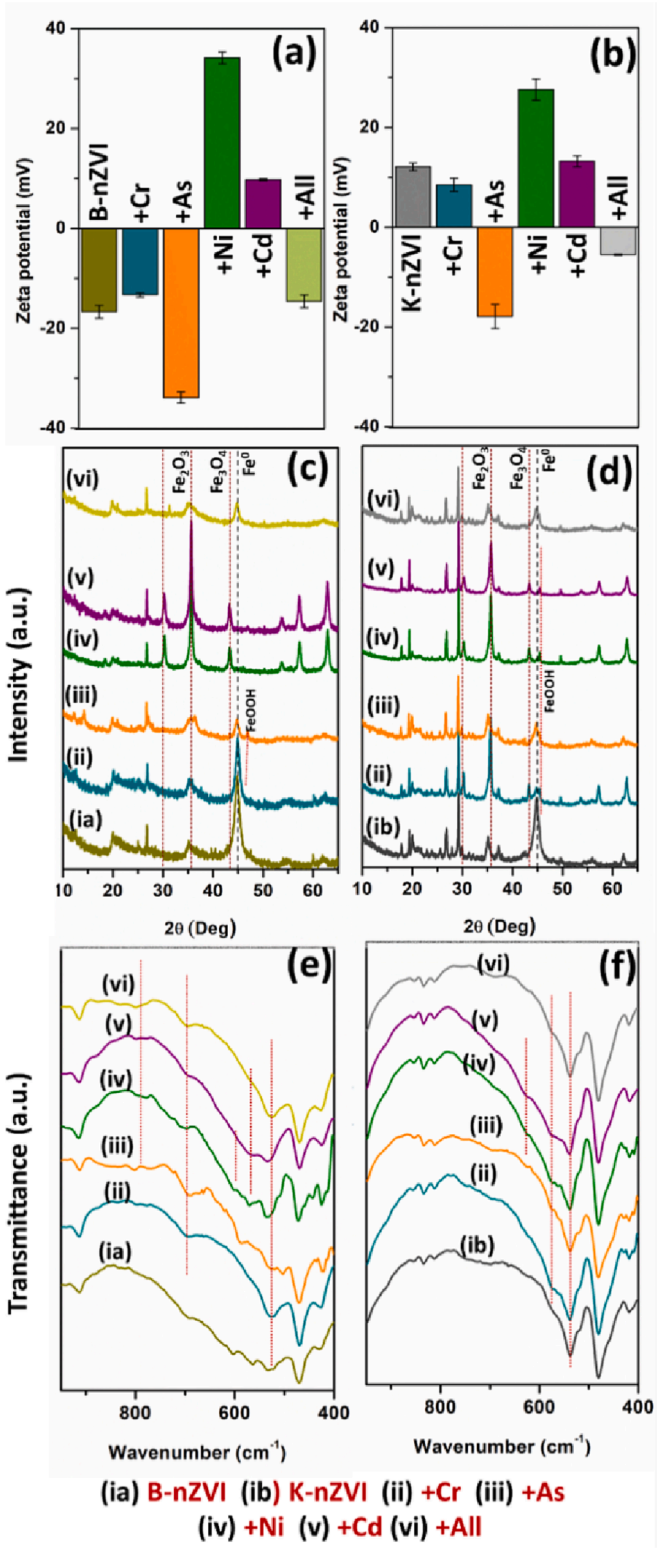

Fig. 3. (a, b) zeta potential, (c, d) pXRD and (e—f) FTIR spectra obtained for different reaction precipitates after sorption experiments using B-nZVI and K-nZVI respectively [(ia) B-nZVI, (ib) K-nZVI, (ii) Cr, (iii) As, (iv) Ni, (v) Cd, and (vi) Cr-As-Ni-Cd].

sections. Results indicate that in the case of B-nZVI, slower CrO_4^{2-} sorption corresponds to initial electrostatic repulsion followed by electron release from Fe^0 and chromate ions reduction and sorption or co-precipitation of Cr(III) on B-nZVI surface. In contrast, K-nZVI showed strong electrostatic attraction of chromate ions on K-nZVI surface, followed by its reduction on the surface via electron transfer from Fe^0 core and attachment of Cr(III) with FeOOH. In multi-metallic solutions, both K-nZVI and B-nZVI showed a decrease in Cr2p peaks intensity with a decrease in Cr(III) abundance to 71% and 68%, respectively (Fig. 4f).

3.2.2. Arsenic

After the sorption of arsenic, both B-nZVI and K-nZVI showed a drastic decrease of zeta potential from 16.7 ± 1.3 mV and + 12.1 ± 0.7 mV to –33.9 ± 1.1 mV and 17.9 ± 2.4 mV, respectively (Fig. 3a-b). pXRD spectra (Fig. 3c-d) showed a decrease in 44.8^0 Fe^0 peak with a slight increase in 35^0 iron oxide peak and 46^0 FeOOH peak in B-nZVI whereas K-nZVI showed the generation of strong 30^0 and broad 35^0 iron oxide peaks. FTIR spectra showed the generation of 805 cm^{-1} stretching due to FeOOH in B-nZVI along with 530 cm^{-1} and 580 cm^{-1} Fe-O stretching (Fig. 8e—f).

XPS spectra (Fig. 4g) of As3d region showed the presence of As(III) on both B—nZVI and K-nZVI surfaces. The As3d spectrum consists of the As $3d_{5/2}$ and As $3d_{3/2}$ lines, separated by 0.69 eV, area ratio 3:2, assigned to As(III)-O(H) bonding. Redox transformation of As(III) is hard to predict in the multi-metallic system due to the presence of Cr3p signals. However, results suggest dominant As(III) complexation with iron oxy-hydroxide.

The XPS data indicate that arsenic is trivalent as added to solution present in the form of $As(OH)_3$(aq) or $HAsO_2$(aq) species. Arsenic can get oxidized to As(V) in a surface water environment where Eh is higher. The presence of nZVI may lower Eh, and arsenic can be reduced to As (III) at contact with nZVI. Presence of arsenic dominantly in the form of $As(OH)_3$ leads to ligand exchange, and switching from Fe-OH_2^+ to Fe-O-$As(OH)_2$ might explain the decrease in zeta potential.

3.2.3. Nickel

Both B-nZVI and K-nZVI showed a change in zeta potential to higher positive value. A drastic increase in zeta potential from 16.7 ± 1.3 mV to + 34.2 ± 1.2 mV in B-nZVI justifies high electrostatic attraction of Ni^{2+} (Fig. 3a-b). Further, pXRD spectra (Fig. 3c-d) showed the generation of 30^0 and 35^0, and 43^0 intense iron oxide peaks and complete disappearance of Fe^0 peak in B—nZVI and presence with very low intensity in K-nZVI. Observation suggests formation of a very thick iron oxide shell on Fe^0 core. FTIR spectra (Fig. 4e-f) further supported this observation and showed generation of 530 cm^{-1}, 570 cm^{-1}, and 630 cm^{-1} Fe—O stretching along with 705 cm^{-1} and 805 cm^{-1} bands due to FeOOH. Standard redox potential of Ni^{2+}/Ni^0 is 0.26 V at 298 K and is well above Fe^{2+}/Fe^0 (0.44 V, 298 K) potential which suggest probable reduction of Ni^{2+} in Ni^0 [50]. But, Ni2p XPS spectra (Fig. 4h) showed presence of Ni(II) peak in the region of 854.9 eV corresponding to Ni $(OH)_2$ suggesting complexation and co-precipitation of nickel.

3.2.4. Cadmium

Similar to nickel, Cd^{2+} sorption also resulted in an increase in zeta potential from 16.7 ± 1.3 mV to + 9.7 ± 0.2 mV in B-nZVI suggested strong electrostatic attraction (Fig. 3a). Whereas, only a slight increase in zeta potential value from + 12.1 ± 0.7 mV to + 13.1 ± 1.1 mV was observed in K-nZVI (Fig. 3b). pXRD and FTIR observations were also similar to nickel, where intense iron-oxide shell generation was observed in the system. Cd3d XPS spectra (Fig. 4i) showed the presence of Cd(II) in the system. Standard redox potential of Cd^{2+}/Cd^0 is 0.40 V at 298 K and is very near to Fe^{2+}/Fe^0 (0.44 V, 298 K) potential suggesting no reduction of cadmium and probable removal via electrostatic attraction, complexation, and co-precipitation of cadmium.

In summary, dominant removal mechanisms were reductive co-precipitation of chromium, complexation of arsenic, electrostatic attraction and co-precipitation of nickel and cadmium with generated iron-oxy-hydroxide shell.

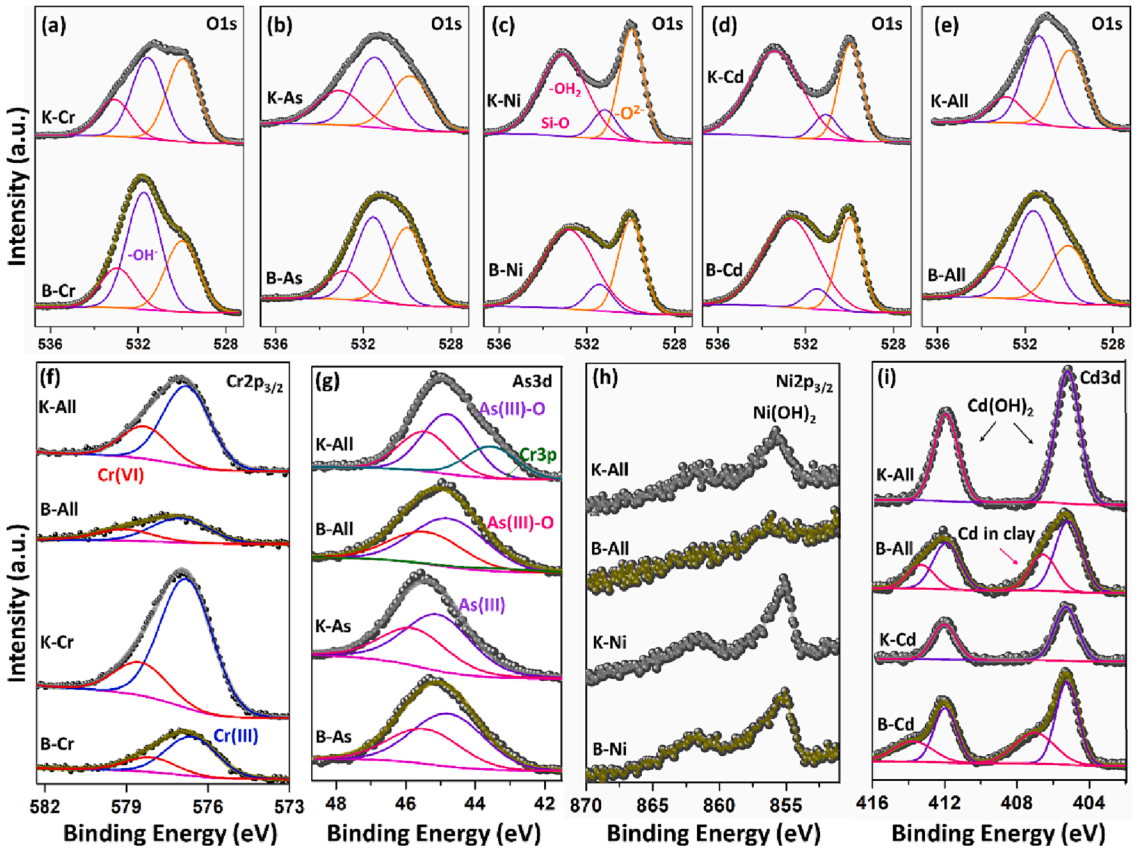

Fig. 4. XPS data for different nanocomposites and reaction precipitates showing fitted (a-e) O1s spectra for reaction residues before and after sorption experiments for B-nZVI and K-nZVI, respectively, and spectral fits for (f) $Cr2p_{3/2}$, (g) As3d, (h) $Ni2p_{3/2}$, and (i) Cd3d regions.

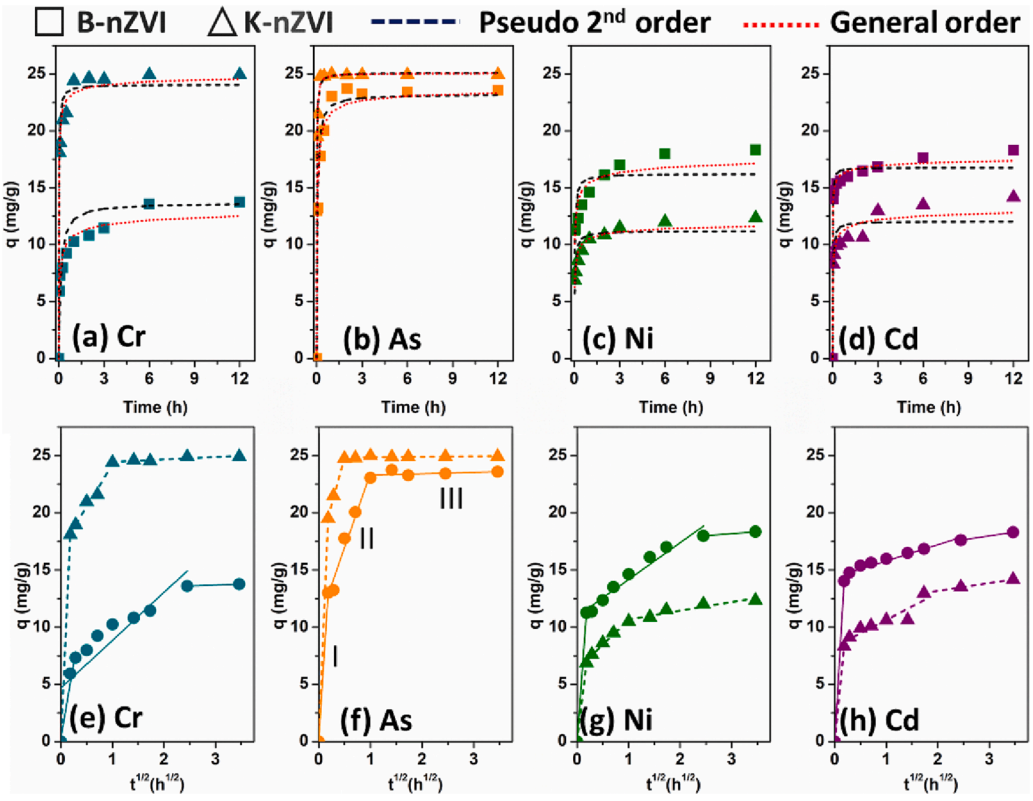

Fig. 5. (a-d) effect of interaction time, reaction kinetics modeling and (e-h) intra-particle diffusion (IPD) modeling of B-nZVI and K-nZVI for mono-ionic contaminant system [C_0 = 20 mg/L, V = 25 mL, m = 20 mg, 200 RPM and 25 °C].

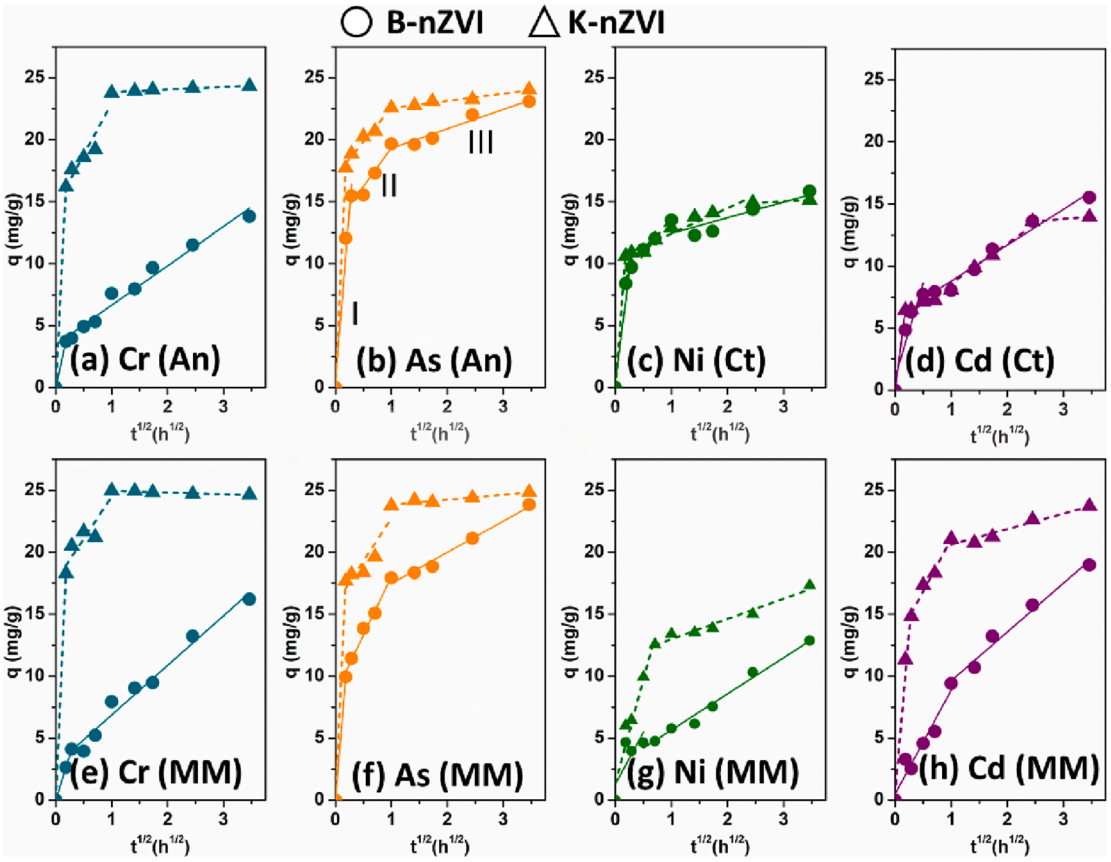

Fig. 6. Intra particle diffusion modeling for B-nZVI and K-nZVI in (a-d) co-ionic and (e-h) multi-ionic contaminant systems [m = 20 mg, V = 20 mL, C_0 = 20 mg/L each, T = 25 °C, RPM = 200, pH = 6.5, t = 0–12 h].

3.3. Sorption behavior in different contaminant systems: Removal kinetics

3.3.1. Mono-ionic contaminant exposure

Aqueous solutions contaminated with single ionic species were reacted with both B-nZVI and K-nZVI to test the comparative preference of nanocomposites. Results in Fig. 5 a-d show that sorption equilibrium was achieved within 3 h of interaction time for all contaminants.

K-nZVI achieved sorption equilibrium faster for chromium (~1h) and arsenic (~10 min) compared to B-nZVI (~6h and 1 h, respectively). In addition, 75% removal of chromium was achieved within 2 min of interaction with K-nZVI, whereas it was only 24% for B-nZVI. Arsenic removal was 78% within 2 min of interaction with K-nZVI compared to 52% for B-nZVI. After equilibration, near complete removal of chromium and arsenic was observed with K-nZVI but not with B-nZVI. Oppositely, B-nZVI showed faster removal of cadmium (56%) and nickel (45%) within 2 min of interaction compared to K-nZVI (27% of nickel and 33% of cadmium). These observations conclude preferential and quasi-instantaneous removal of anionic species with positively charged K-nZVI and cationic species with negatively charged B-nZVI due to both favored chemical binding and electrostatic attractions.

Insights on adsorption kinetics were obtained through kinetic modeling of experimental data using pseudo-second order and general order models. The first one presumes the order of a reaction to be 2 whereas the latter suggests that the order of a reaction shouldn't be presumed but calculated using experimental data [51].

Therefore, the general order model provides information about equilibrium sorption capacity, rate constant, and reaction order and is a three-parameter model [52]. Models fit in Fig. 5 a-d and obtained parameters in table S3 show that the general order model fits well compared to pseudo-second order for all contaminants and therefore justifies varying reaction orders for different contaminants. The reaction order ranged from 2 to 5, suggesting that both nanocomposites follow higher order kinetics for contaminants removal. Intra-particle diffusion (IPD) model in Fig. 5 e-h show three different linear segments corresponding to (i) initial bulk transfer to the adsorbent surface, (ii) diffusion of adsorbate in the *meso*, macro, and micropores, and (iii) final equilibrium stage and, in mono-ionic contaminant systems, the same trend was observed in most of the cases. Here the three segments can be tentatively attributed to faster adsorption followed by redox transformation (for chromium and arsenic) and/or co-precipitation and final equilibrium stage [53]. Intercept values for IPD were in order Cr < As < Ni < Cd for B-nZVI while it was As < Cr < Cd < Ni for K-nZVI suggesting limited bulk transport and comparatively longer IPD stage for chromium and arsenic with B-nZVI than K-nZVI suggesting slower redox transformation and co-precipitation on B-nZVI surface. Whereas, Ni^{2+} and Cd^{2+} exhibited limited bulk transfer and shorter IPD stage on K-nZVI surface compared to B-nZVI, suggesting limited metal cations removal capacity of K-nZVI than B-nZVI.

3.3.2. Co-ionic contaminant exposure

Remediation of water bodies contaminated with multiple similar charged toxicant ions can be of higher environmental relevance compared to mono-ionic contamination. The presence of multiple contaminants can either induce competitive sorption or co-operative sorption and, therefore can impact the total metal sorption capacities of nanocomposites.

To understand the behavior of B-nZVI and K-nZVI in co-ionic systems, nanocomposites were reacted with aqueous solutions contaminated with Cr-As and Ni-Cd to represent anionic (An) and cationic (Ct) systems, respectively. Similar to mono-ionic system, K-nZVI showed faster and higher removal of both chromium and arsenic (Fig. S7 a-b). Parameters obtained from well fitted general order model provide

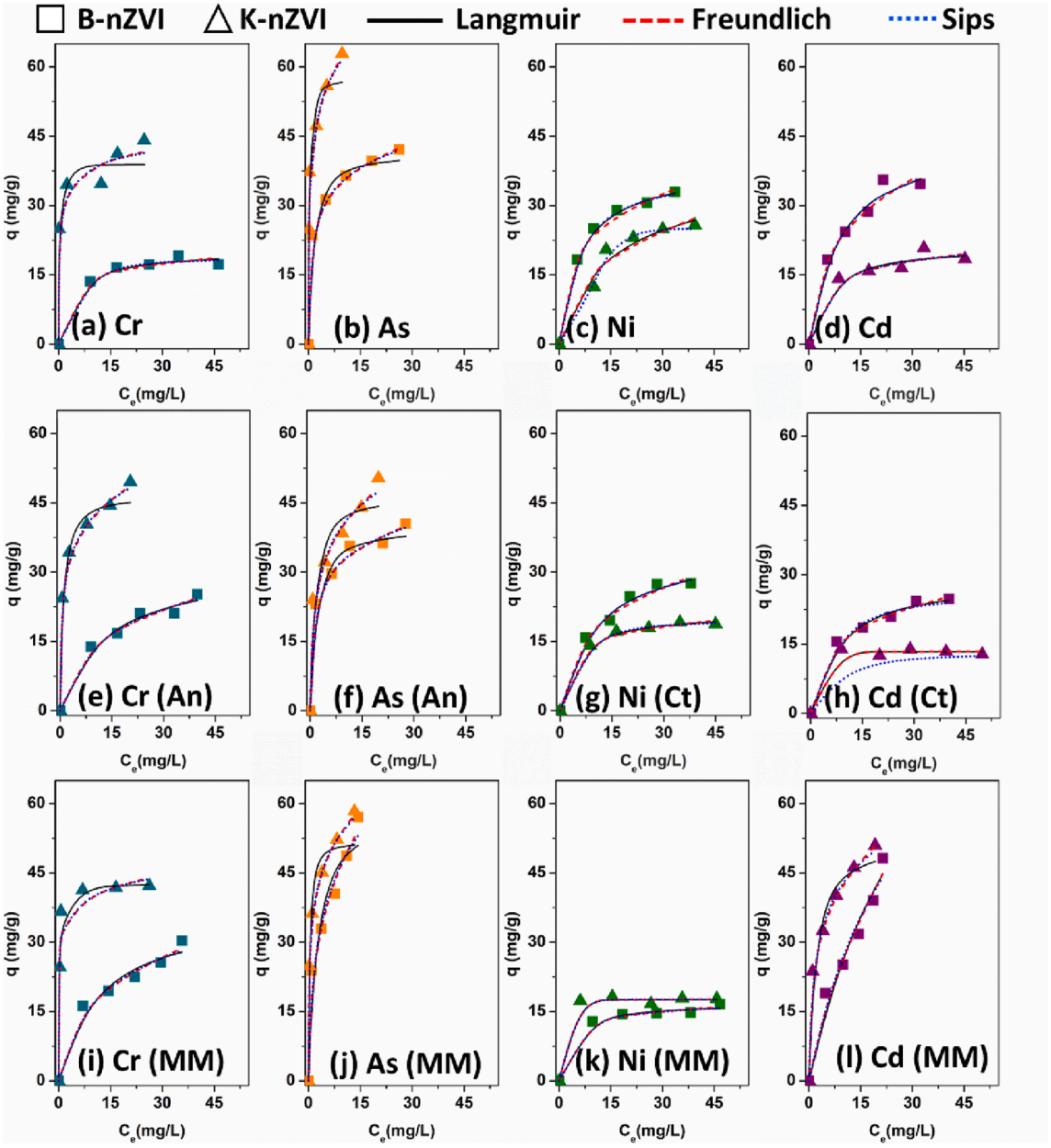

Fig. 7. Impact of varying contaminants concentration on sorption capacity of B-nZVI and K-nZVI nanocomposites and sorption isotherm modeling in (a-d) mono-ionic, (e-h) co-ionic and (i-l) multi-ionic contaminant solutions [m = 20 mg, V = 20 mL, C_0 = 10–75 mg/L, T = 25 °C, RPM = 200, pH = 6.5, t = 12 h, An = Cr + As, Ct = Ni + Cd, MM = Cr + As + Ni + Cd].

reaction order in the range of 3–5 (Table S3b). IPD modeling in Fig. 6 a-d also show higher bulk transport of chromium and arsenic to the K-nZVI surface compared to B—nZVI. Equilibrium was not achieved completely in case of B-nZVI for both chromium and arsenic suggesting removal at a slower rate. In comparison to mono-ionic system, removal of Ni^{2+} and Cd^{2+} decreased slightly for B-nZVI in co-contaminant system (Fig. S7 c-d). Corresponding to near equal bulk transfer and similar IPD curve slope, both K-nZVI and B-nZVI showed removal of Ni^{2+} and Cd^{2+} at a near equal rate (Fig. 6 c-d). These observations further suggest a simultaneous increase in the cations removal capacity for K-nZVI in co-ionic system containing nickel and cadmium.

3.3.3. *Multi-ionic contaminant exposure*

Water streams can receive toxic ions through several anthropogenic activities including wastes from different industrial outlets that can contaminate river and groundwater bodies with multiple ionic species. Therefore, it is essential to test the efficiency and behavior of synthesized nanocomposites in multi—ionic contaminant solutions. Here, multi-contaminant solutions contain equal concentrations of chromium, arsenic, nickel, and cadmium.

The simultaneous presence of both cationic and anionic contaminant species led to drastic variations in the sorption behavior of B-nZVI and K-nZVI compared to mono-ionic solutions (Fig. S7 e-h). Enhanced sorption of oxy-anions was observed but with the limited bulk transfer of adsorbate and longer and slower IPD stage in B-nZVI. In addition, no sorption equilibrium was achieved in B-nZVI in the studied time frame of 12 h (Fig. S7 e-h). IPD model (Fig. 6 e-h) showed the change in intercept values of B-nZVI and K-nZVI from 3.4 mg/g and 14.6 mg/g to 4.6 mg/g and 16.8 mg/g for chromium in multi-contaminant system, suggesting enhanced bulk transport of chromium on both B-nZVI and K-nZVI surfaces. Whereas arsenic showed a slight decrease in IPD intercept i.e., from 10.4 mg/g and 16.6 mg/g to 8.6 mg/g and 15.8 mg/g. At the same

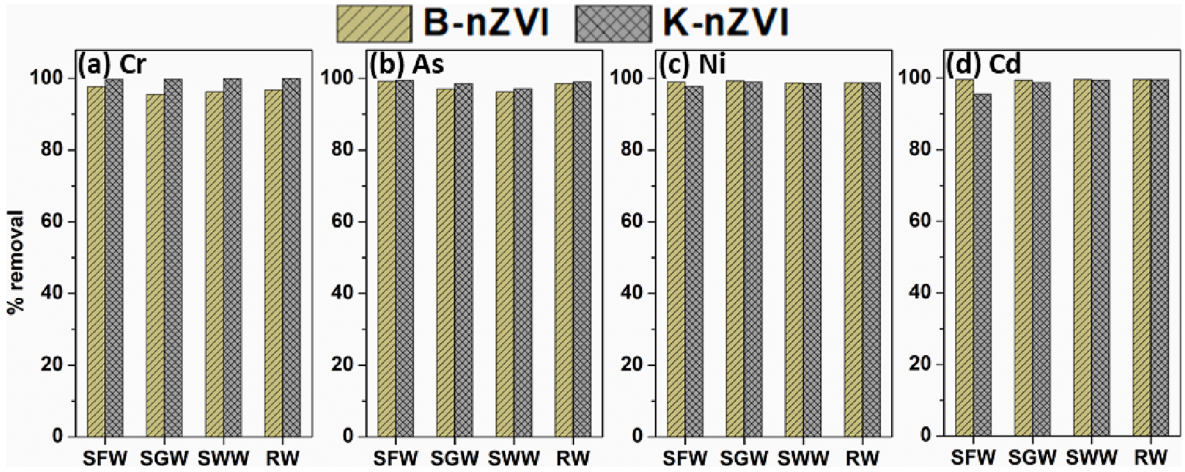

Fig. 8. Removal of various metallic species from different aqueous matrices [m = 20 mg, V = 20 mL, C_0 = 10 mg/L, T = 25 °C, RPM = 200, t = 12 h, SFW = synthetic fresh water, SGW = synthetic groundwater, SWW = synthetic wastewater, RW = river water].

time, B-nZVI showed a drastic decrease in bulk transport of Ni^{2+} (from 10.9 mg/g to 2.7 mg/g) and Cd^{2+} (14.4 mg/g to 5.7 mg/g), suggesting initial sorption sites competition between nickel and cadmium on B-nZVI surface [54]. K-nZVI showed enhanced intercept values from 6.3 mg/g to 11.3 mg/g for Ni^{2+} and 8.3 mg/g to 12.6 mg/g for Cd^{2+} suggesting co-operative effects. The mechanism can further be supported using observations from mono-ionic solutions, which showed faster sorption of oxy-anions on K-nZVI that caused B-nZVI zeta potential to decrease from + 12.1 ± 0.7 mV to + 8.5 ± 1.3 mV for chromium and to –33.9 ± 1.1 mV for arsenic. Similarly, in multi-ionic contaminated solutions, initial faster attraction of oxy-anions to K-nZVI surface turned the surface charge to negative and creates an electrostatically favorable environment for heavy metal cations. In stage-2, electron transfer from nZVI led to redox-transformation of chromium, and strong complexation of arsenic and co-precipitation of nickel and cadmium as confirmed using XPS and FTIR analysis. Fitting of experimental data in non-linear kinetic models also showed comparatively best fit with general order where the order of reaction was found in range of 2–6 (Table S3c).

3.4. *Impact of varying contaminant concentrations*

Mono-contaminant aqueous solutions of varying concentrations of respective contaminants were reacted with nanocomposites to understand the impact of increasing contaminant concentration on the sorption capacities of B-nZVI and K-nZVI. Results in Fig. 7 a-d shows an increase in the sorption capacity of nanocomposites with increasing contaminant's concentration followed by plateau formation with the saturation of sorption sites. K-nZVI showed continuous increase in sorption capacities for chromium and arsenic oxy-anions while B-nZVI formed a plateau for chromium and showed a comparatively slower increase in arsenic sorption capacity. In contrast, K-nZVI showed site saturation and formation of plateau for Ni^{2+} and Cd^{2+} whereas higher removal capacity and continuous increase in sorption capacity of B-nZVI was observed for cationic species.

To obtain information about maximum sorption capacities, nature of adsorbent surface, and removal mechanisms, non-linear sorption isotherm modeling using Langmuir, Freundlich, and Sips models was performed. In general, Langmuir isotherm assumes monolayer sorption with homogeneous nature of adsorbent surface, whereas Freundlich assumes a heterogeneous surface and multi-layer stacking of adsorbate molecules [55]. Both of these isotherms are two-parameter models whereas Sips isotherm which is a combination of Freundlich (at low concentrations) and Langmuir (at higher concentrations) isotherms, is a three-parameter model [56]. Further description of sorption isotherm models is provided in the section 3 of supplementary information. Results in Fig. 7 a-d and parameters in Table S4a show that Sips isotherm best fits all the contaminants, confirming the heterogeneous nature of both nanocomposites. In all cases, 'n' / 1 further confirmed the heterogeneous nature of composites surface. Obtained maximum sorption capacities of B-nZVI for chromium and arsenic were 18.4 mg/g and 86.8 mg/g which were comparatively lesser than K-nZVI i.e., 87.4 mg/g for chromium and 157.3 mg/g for arsenic. In contrast, B-nZVI showed higher sorption capacities for Ni^{2+} (36 mg/g) and Cd^{2+} (46 mg/g) compared to K-nZVI (25 mg/g and 27 mg/g, respectively). These experimental observations further confirm preferential sorption of cationic species on B-nZVI and anionic species on K-nZVI surface.

Similar preferential behavior of B-nZVI and K-nZVI was observed in co-ionic contaminant solutions (Fig. 7 e-h). While B-nZVI showed a slight increase in sorption capacities for chromium (51.1 mg/g) and arsenic (98.2 mg/g), it was still lower than K-nZVI (126.9 mg/g and 121.3 mg/g, respectively). This may be attributed to enhanced aging of B-nZVI in the presence of co-anionic solutions and suggests co-operative effects of oxy-anions. In contrast, a decrease in respective sorption capacities of Ni^{2+} and Cd^{2+} was observed for both nanocomposites suggesting competitive effects in the presence of metal cations. The simultaneous presence of Cr(III) and As(III) can lead to the formation of ternary complexes leading to their higher sorption capacities. Therefore, total anion sorption capacities were 149.33 mg/g and 248.3 mg/g for B-nZVI and K-nZVI, respectively, which were comparatively higher than the individual chromium and arsenic removal capacities of nanocomposites. Similarly, total cation sorption capacities were 32.9 mg/g (B-nZVI) and 63.4 mg/g (K-nZVI) and were slightly higher than the individual cation sorption capacities of respective nanocomposites. This slight increase can be attributed to the impact of enhanced total contaminant load in the system leading to higher sorption on heterogeneous surfaces of composites.

Similarly, the simultaneous presence of both anionic and cationic contaminants led to increased total metal sorption capacities of nanocomposites (Fig. 7 e-l). Obtained parameters from well-fitted Sips isotherm model (Table S4c) have shown higher sorption capacities of K-nZVI for anions i.e., chromium (62.2 mg/g and 98.1 mg/g) and arsenic (131.6 mg/g and 169.6 mg/g), respectively for B-nZVI and K-nZVI. In the case of cationic species, B-nZVI showed higher sorption capacities than K-nZVI for both Ni^{2+} (20.1 mg/g and 17.7 mg/g) and Cd^{2+} (113.2 mg/g and 87.1 mg/g). Sorption capacity for cadmium increased drastically of both nanocomposites, compared to mono and co-ionic solutions. Interestingly, total maximum contaminant sorption capacities of both B-nZVI (327 mg/g) and K-nZVI (372 mg/g) were several folds higher than mono-ionic sorption capacities. A comparison of sorption capacities of earlier reported adsorbents is provided in Table S6 of

supplementary information. This behavior can again be attributed to enhanced co-operative effects due to the presence of both cations and oxy-anions in the system that can facilitate multi-layer stacking, ternary complexation, and co-precipitation in the system, leading to enhanced removal of contaminants. Thermodynamic calculations (Table S5) showed that ΔG values were negative in all the cases and mostly < -20 kJ/mol suggesting reaction spontaneity and chemisorption characteristics [57,58].

3.5. Effect of solution pH

Attributing to the high sorption affinity of B-nZVI for cationic species and K-nZVI for anionic contaminants, similar preferential sorption behavior was observed at varying pH as well (Fig. S8 a-l). Therefore, in the studied pH range of 3.5 to 10, K-nZVI showed comparatively higher sorption capacity for chromium and arsenic, whereas B-nZVI showed higher removal of Ni^{2+} and Cd^{2+} in mono-ionic and co-ionic contaminant exposure. A slight decrease in the sorption of anionic species at alkaline pH can be attributed to negative surface charge of both B-nZVI and K-nZVI that led to electrostatic repulsion in the system with anionic contaminant species and unfavorable ligand exchange (OH^-) reactions in basic conditions. For example, As(III) prevails as $As(OH)_3$ at pH < 9 which behaves like a ligand and can undergo ligand exchange reactions with OH^- on Fe-OH surface sites. This reaction is facilitated on positively charged (i.e. protonated) surface sites ($Fe\text{-}OH_2^+$) because surface H_2O groups are more easily exchanged than OH^- leading to pH-dependent decreasing adsorption of As(III) on nanocomposites surface.

In contrast, we observed an increase in the sorption capacity for cationic species with an increase in pH, which may also be attributed to the formation of insoluble metal hydroxide species at very alkaline conditions (pH 10). Interestingly, in the multi-ionic system, K-nZVI has shown higher sorption of all the contaminants in the studied pH range (3.5–10) that can be attributed to all the cooperative effects as described in previous sections. In the case of a highly acidic environment (pH 3.5), nanocomposites have shown a decrease in the sorption capacity for all the contaminants, which may be due to the leaching of formed Fe^{2+}, resulting in slight desorption of contaminants.

3.6. Environmental applications: Contaminant preference in complex water matrices

It is a critical challenge for adsorbents to remove the trace amounts of contaminants and to keep the contaminant concentration below the drinking water permissible limit in environmental water samples. The observed variation in the growth behavior of nZVI particles on different clay surfaces that led to their respective preferential behavior and higher sorption capacities for electrostatically favored contaminants allowed further investigation on their behavior in different complex water matrices. For that, four different waters, i.e., synthetic groundwater, synthetic freshwater, synthetic wastewater, and natural river water, were spiked with 10 mg/L of each contaminant (Cr, As, Ni, and Cd) together.

Interestingly, results have shown (Fig. 8 a-d) that both the nanocomposites were able to remove all the contaminants to > 98% in all studied water matrices. Observed concentration of different contaminants in various elutes shown that K-nZVI was able to remediate water for chromium and arsenic oxy-anions below permissible limits, whereas B-nZVI succeeded in sequestering Ni^{2+} and Cd^{2+} up to drinking water standards as set by WHO, in all studied types of complex aqueous matrices.

3.7. Environmental applications: Secondary iron release

Fe^0 oxidation and secondary release of iron ions and sorbed contaminants is a big challenge for the commercialization of nZVI based solutions for water purification and wastewater treatment. Here, we have monitored iron release during all sorption experiments with both nanocomposites. Results in Fig. S9 show that both the nanocomposites have prevented iron release below its permissible limit of 2 mg/L. Moreover, the mean values of iron release were 0.012 mg/L for B-nZVI and 0.038 mg/L for K-nZVI. Obtained most extreme outliers were in case of high acidic solutions i.e., pH 3.5 in both cases. Results confirm that considering preferential sorption of specific ionic species, B-nZVI and K-nZVI can be applied to higher cationic-low anionic contamination and higher anionic-low cationic contamination systems, respectively for sustainable water treatment.

4. Conclusions

The study concludes that varying crystal structures and surface properties of clays lead to different growth behavior of redox-sensitive nZVI particles on these supporting surfaces. Here, swelling bentonite showed Fe^0 nanoparticles growth both in the interlayers and on the surface while only surface attachment was observed in non-swelling kaolinite. Variation in growth behavior altered various surface properties of formed B-nZVI and K-nZVI nanocomposites such as nanoparticles size, surface area, zeta potential, etc. These surface variations resulted in selectively higher sorption of electrostatically favored species on respective nanocomposites, i.e., positively charged K-nZVI for chromium and arsenic oxy-anions (87.47 and 157.35 mg/g) than of negatively charged B-nZVI (18.44 and 86.88 mg/g). Oppositely, B-nZVI has shown higher sorption of metal cations Ni^{2+} and Cd^{2+} (36 mg/g and 46 mg/g) than K-nZVI (25 and 27 mg/g). Detailed characterization of reaction precipitates suggested reductive co-precipitation of Cr(VI), complexation of As(III), complexation and co-precipitation of Ni^{2+} and Cd^{2+} with generated iron-oxy—hydroxides were the major contaminant removal mechanisms with co-operative effects in multi-ionic contaminated solutions. Sorption capacities ranged to 327 mg/g and 372 mg/g for B-nZVI and K-nZVI, respectively in multi-contaminant solutions, justifying higher total metal sorption capacities of both nanocomposites.

nZVI growth variation on different clay surfaces has also shown a significant implication in drinking water purification and wastewater treatment, where we observed the ability of B-nZVI and K-nZVI to remediate cationic and anionic metal species, respectively, below the WHO-defined maximum permissible limits from freshwater, groundwater, river water and wastewater like complex aqueous matrices. Overall, this study concludes that the surface dependent variation in the growth of redox-sensitive nanoparticles can lead to a variation in their surface properties, resulting in preferentially higher removal of specific ionic species than others. Designed nanocomposites i.e., B-nZVI and K-nZVI can be used to remediate higher metal cations- low oxy-anions and low metal cations- high oxy-anions contaminated water bodies, respectively.

Declaration of Competing Interest

The authors declare that they have no known competing financial interests or personal relationships that could have appeared to influence the work reported in this paper.

Data availability

No data was used for the research described in the article.

Acknowledgments

Authors would like to acknowledge the financial support from the SERB-ECR project grant (ECR/2017/000707) and the SERB-CRG project grant (CRG/2021/006020) from Department of Science and Technology (DST), India. Central instrumentation facility of the Indian Institute of Science Education and Research Kolkata should be acknowledged for providing nanocomposites characterization instruments (BET, ICP-OES,

FESEM, TEM, pXRD, and XRF). Nisha Singh and Nitin Khandelwal also want to acknowledge the IISER-K research fellowships.

Appendix A. Supplementary data

Supplementary data to this article can be found online at https://doi.org/10.1016/j.cej.2023.141883.

References

[1] W. UNESCO, The United Nations world water development report 2019: Leaving no one behind, UNESCO Paris, 2019.

[2] A. Boretti, L. Rosa, Reassessing the projections of the World Water Development Report, Npj Clean Water 2 (2019). https://doi.org/UNSP 15 10.1038/s41545-019-0039-9.

[3] H. Ali, E. Khan, Ikram Ilahi, Environmental Chemistry and Ecotoxicology of Hazardous Heavy Metals: Environmental Persistence, Toxicity, and Bioaccumulation, J. Chem. 2019 (2019), 6730305, https://doi.org/10.1155/2019/6730305.

[4] R.E. Engler, The complex interaction between marine debris and toxic chemicals in the ocean, Environ Sci Technol 46 (22) (2012) 12302–12315, https://doi.org/10.1021/es3027105.

[5] S. Rajeshkumar, X. Li, Bioaccumulation of heavy metals in fish species from the Meiliang Bay, Taihu Lake, China, Toxicol. Rep. 5 (2018) 288–295, https://doi.org/10.1016/j.toxrep.2018.01.007.

[6] R.J. Reeder, M.A.A. Schoonen, A. Lanzirotti, Metal speciation and its role in bioaccessibility and bioavailability, Rev. Mineral. Geochem. 64 (1) (2006) 59–113, https://doi.org/10.2138/rmg.2006.64.3.

[7] S.J. Hug, L. Canonica, M. Wegelin, D. Gechter, U. von Gunten, Solar oxidation and removal of arsenic at circumneutral pH in iron containing waters, Environ Sci Technol 35 (10) (2001) 2114–2121, https://doi.org/10.1021/es001551s.

[8] Z. Wang, R.T. Bush, L.A. Sullivan, J. Liu, Simultaneous redox conversion of chromium(VI) and arsenic(III) under acidic conditions, Environ Sci Technol 47 (12) (2013) 6486–6492, https://doi.org/10.1021/es400547p.

[9] Z. Hu, K. Chandran, D. Grasso, B.F. Smets, Effect of nickel and cadmium speciation on nitrification inhibition, Environ Sci Technol 36 (14) (2002) 3074–3078, https://doi.org/10.1021/es015784a.

[10] M.A. Barakat, New trends in removing heavy metals from industrial wastewater, Arab J Chem 4 (4) (2011) 361–377, https://doi.org/10.1016/j.arabjc.2010.07.019.

[11] K.R. Reddy, Technical challenges to in-situ remediation of polluted sites, Geotech. Geol. Eng. 28 (3) (2010) 211–221, https://doi.org/10.1007/s10706-008-9235-y.

[12] S. Bolisetty, M. Peydayesh, R. Mezzenga, Sustainable technologies for water purification from heavy metals: review and analysis, Chem Soc Rev 48 (2) (2019) 463–487, https://doi.org/10.1039/C8CS00493E.

[13] C.C. Azubuike, C.B. Chikere, G.C. Okpokwasili, Bioremediation techniques–classification based on site of application: principles, advantages, limitations and prospects, World J. Microbiol. Biotechnol. 32 (11) (2016) 180, https://doi.org/10.1007/s11274-016-2137-x.

[14] N.L. Le, S.P. Nunes, Materials and membrane technologies for water and energy sustainability, Sustain Mater Techno 7 (2016) 1–28, https://doi.org/10.1016/j.susmat.2016.02.001.

[15] S. De Gisi, G. Lofrano, M. Grassi, M. Notarnicola, Characteristics and adsorption capacities of low-cost sorbents for wastewater treatment: A review, Sustainable, Mater. Technol. 9 (2016) 10–40, https://doi.org/10.1016/j.susmat.2016.06.002.

[16] N. Khandelwal, E. Tiwari, N. Singh, R. Marsac, T. Schafer, F.A. Monikh, G. K. Darbha, Impact of long-term storage of various redox-sensitive supported nanocomposites on their application in removal of dyes from wastewater: mechanisms delineation through spectroscopic investigations, J Hazard Mater (2020), 123375, https://doi.org/10.1016/j.jhazmat.2020.123375.

[17] S. Mondal, U. Rana, S. Malik, Reduced graphene oxide/Fe_3O_4/polyaniline nanostructures as electrode materials for an all-solid-state hybrid supercapacitor, J. Phys. Chem. C 121 (14) (2017) 7573–7583, https://doi.org/10.1021/acs.jpcc.6b10978.

[18] B.P. von der Heyden, A.N. Roychoudhury, Application, chemical interaction and fate of iron minerals in polluted sediment and soils, Curr. Pollut. Rep. 1 (4) (2015) 265–279, https://doi.org/10.1007/s40726-015-0020-2.

[19] Y. Zou, X. Wang, A. Khan, P. Wang, Y. Liu, A. Alsaedi, T. Hayat, X. Wang, Environmental remediation and application of nanoscale zero-valent iron and its composites for the removal of heavy metal ions: a review, Environ Sci Technol 50 (14) (2016) 7290–7304, https://doi.org/10.1021/acs.est.6b01897.

[20] X. Guan, Y. Sun, H. Qin, J. Li, I.M. Lo, D. He, H. Dong, The limitations of applying zerovalent iron technology in contaminants sequestration and the corresponding countermeasures: the development in zerovalent iron technology in the last two decades (1994–2014), Water Res 75 (2015) 224–248, https://doi.org/10.1016/j.watres.2015.02.034.

[21] N. Khandelwal, N. Singh, E. Tiwari, G.K. Darbha, Novel synthesis of a clay supported amorphous aluminum nanocomposite and its application in removal of hexavalent chromium from aqueous solutions, Rsc Adv 9 (20) (2019) 11160–11169, https://doi.org/10.1039/C9RA00742C.

[22] N. Ezzatahmadi, G.A. Ayoko, G.J. Millar, R. Speight, C. Yan, J.H. Li, S.Z. Li, J. X. Zhu, Y.F. Xi, Clay-supported nanoscale zerovalent iron composite materials for the remediation of contaminated aqueous solutions: A review, Chem. Eng. J. 312 (2017) 336–350, https://doi.org/10.1016/j.cej.2016.11.154.

[23] G. Sposito, N.T. Skipper, R. Sutton, S.-h. Park, A.K. Soper, J.A. Greathouse, Surface geochemistry of the clay minerals, Proc. Natl. Acad. Sci. U.S.A. 96 (7) (1999) 3358–3364.

[24] L.N. Shi, Y.M. Lin, X. Zhang, Z.L. Chen, Synthesis, characterization and kinetics of bentonite supported nZVI for the removal of Cr(VI) from aqueous solution, Chem Eng J 171 (2) (2011) 612–617, https://doi.org/10.1016/j.cej.2011.04.038.

[25] Ç. Üzüm, T. Shahwan, A.E. Eroğlu, K.R. Hallam, T.B. Scott, I. Lieberwirth, Synthesis and characterization of kaolinite-supported zerovalent iron nanoparticles and their application for the removal of aqueous Cu^{2+} and Co^{2+} ions, Appl. Clay Sci. 43 (2) (2009) 172–181, https://doi.org/10.1016/j.clay.2008.07.030.

[26] J. Wang, G.J. Liu, T.F. Li, C.C. Zhou, C.C. Qi, Zero-valent iron nanoparticles (NZVI) supported by kaolinite for Cu-II and Ni-II ion removal by adsorption: kinetics: thermodynamics, and mechanism, Aust. J. Chem. 68 (8) (2015) 1305–1315, https://doi.org/10.1071/Ch14675.

[27] A. Baldermann, S. Kaufhold, R. Dohrmann, C. Baldermann, I. Letofsky-Papst, M. Dietzel, A novel nZVI–bentonite nanocomposite to remove trichloroethene (TCE) from solution, Chemosphere 282 (2021), 131018, https://doi.org/10.1016/j.chemosphere.2021.131018.

[28] G. Sheng, X. Shao, Y. Li, J. Li, H. Dong, W. Cheng, X. Gao, Y. Huang, Enhanced removal of uranium(VI) by nanoscale zerovalent iron supported on na–bentonite and an investigation of mechanism, Chem. A Eur. J. 118 (16) (2014) 2952–2958, https://doi.org/10.1021/jp412404w.

[29] I. Aksu, E. Bazilevskaya, Z.T. Karpyn, Swelling of clay minerals in unconsolidated porous media and its impact on permeability, GeoResJ 7 (2015) 1–13, https://doi.org/10.1016/j.grj.2015.02.003.

[30] C.L.G. Amorim, R.T. Lopes, R.C. Barroso, J.C. Queiroz, D.B. Alves, C.A. Perez, H. R. Schelin, Effect of clay–water interactions on clay swelling by X-ray diffraction, Nucl. Instrum. Methods Phys. Res., Sect. A 580 (1) (2007) 768–770, https://doi.org/10.1016/j.nima.2007.05.103.

[31] E.M. Araujo, A.M.D. Leite, R.A.d. Paz, V.d.N. Medeiros, T.J.A.d. Melo, H.d.L. Lira, Polyamide 6 Nanocomposites with Inorganic Particles Modified with Three Quaternary Ammonium Salts, Materials (Basel) 4 (11) (2011) 1956–1966, https://doi.org/10.3390/ma4111956.

[32] Y.-H. Son, J.-K. Lee, Y. Soong, D. Martello, M. Chyu, Structure−property correlation in iron oxide nanoparticle−clay hybrid materials, Chem. Mater. 22 (7) (2010) 2226–2232, https://doi.org/10.1021/cm9024843.

[33] A. Sachan, D. Penumadu, Identification of microfabric of kaolinite clay mineral using X-ray diffraction technique, Geotech. Geol. Eng. 25 (6) (2007) 603, https://doi.org/10.1007/s10706-007-9133-8.

[34] S. Bae, R.N. Collins, T.D. Waite, K. Hanna, Advances in surface passivation of nanoscale zerovalent iron: A critical review, Environ Sci Technol 52 (21) (2018) 12010–12025, https://doi.org/10.1021/acs.est.8b01734.

[35] N. Khandelwal, M.P. Behera, J.K. Rajak, G.K. Darbha, Biochar–nZVI nanocomposite: optimization of grain size and Fe0 loading, application and removal mechanism of anionic metal species from soft water, hard water and groundwater, Clean Technol. Envir. 22 (5) (2020) 1015–1024.

[36] F. Huber, D. Schild, T. Vitova, J. Rothe, R. Kirsch, T. Schafer, U(VI) removal kinetics in presence of synthetic magnetite nanoparticles, Geochim. Cosmochim. Ac. 96 (2012) 154–173, https://doi.org/10.1016/j.gca.2012.07.019.

[37] K. Yotsuji, Y. Tachi, H. Sakuma, K. Kawamura, Effect of interlayer cations on montmorillonite swelling: Comparison between molecular dynamic simulations and experiments, Appl Clay Sci 204 (2021), 106034, https://doi.org/10.1016/j.clay.2021.106034.

[38] F.T. Madsen, M. Müller-Vonmoos, The swelling behaviour of clays, Appl. Clay Sci. 4 (2) (1989) 143–156, https://doi.org/10.1016/0169-1317(89)90005-7.

[39] X. Zhang, S. Lin, Z. Chen, M. Megharaj, R. Naidu, Kaolinite-supported nanoscale zerovalent iron for removal of Pb^{2+} from aqueous solution: Reactivity, characterization and mechanism, Water Res. 45 (11) (2011) 3481–3488, https://doi.org/10.1016/j.watres.2011.04.010.

[40] L.-N. Shi, X. Zhang, Z.-L. Chen, Removal of Chromium (VI) from wastewater using bentonite-supported nanoscale zerovalent iron, Water Res. 45 (2) (2011) 886–892, https://doi.org/10.1016/j.watres.2010.09.025.

[41] C. Reginatto, I. Cecchin, K.S. Heineck, K.R. Reddy, A. Thomé, Use of nanoscale zero-valent iron for remediation of clayey soil contaminated with hexavalent chromium: batch and column tests, Int. J. Environ. Res. Public Health 17 (3) (2020), https://doi.org/10.3390/ijerph17031001.

[42] M.M. Tarekegn, A.M. Hiruy, A.H. Dekebo, Nano zero valent iron (nZVI) particles for the removal of heavy metals (Cd^{2+}, Cu^{2+} and Pb^{2+}) from aqueous solutions, RSC Adv. 11 (30) (2021) 18539–18551, https://doi.org/10.1039/d1ra01427g.

[43] J. Adusei-Gyamfi, V. Acha, Carriers for nano zerovalent iron (nZVI): synthesis, application and efficiency, RSC Adv. 6 (93) (2016) 91025–91044, https://doi.org/10.1039/C6RA16657A.

[44] A. Kumar, P. Lingfa, Sodium bentonite and kaolin clays: Comparative study on their FT-IR, XRF, and XRD, Mater. Today: Proc. 22 (2020) 737–742, https://doi.org/10.1016/j.matpr.2019.10.037.

[45] C. Wei-Min, H. Xiang-Ming, Z. Yan-Yun, W. Ming-Yue, H. Zun-Xiang, Y. Xing-Teng, Preparation and swelling properties of poly(acrylic acid-co-acrylamide) composite hydrogels, E-Polymers 17 (1) (2017) 95–106, https://doi.org/10.1515/epoly-2016-0250.

[46] A. Liu, W.-X. Zhang, Fine structural features of nanoscale zerovalent iron characterized by spherical aberration corrected scanning transmission electron microscopy (Cs-STEM), Analyst 139 (18) (2014) 4512–4518, https://doi.org/10.1039/C4AN00679H.

[47] D. Niriella, R. Carnahan, Comparison study of zeta potential values of bentonite in salt solutions, J. Disper Sci. Technol. 27 (2005) 123–131, https://doi.org/10.1081/DIS-200066860.
[48] J.F. Moulder, W.F. Stickle, W.M. Sobol, K.D. Bomben, Handbook of X-ray photoelectron, Spectroscopy (1992).
[49] A. Kraut-Vass, C.J. Powell, S.W. Gaarenstroom, NIST X-ray photoelectron spectroscopy database, Measurement Services Division of the National Institute of Standards and …2012.
[50] P. Acharya, Z.J. Nelson, M. Benamara, R.H. Manso, S.I.P. Bakovic, M. Abolhassani, S. Lee, B. Reinhart, J. Chen, L.F. Greenlee, Chemical structure of Fe–Ni nanoparticles for efficient oxygen evolution reaction electrocatalysis, ACS Omega 4 (17) (2019) 17209–17222, https://doi.org/10.1021/acsomega.9b01692.
[51] É.C. Lima, M.A. Adebayo, F.M. Machado, Kinetic and equilibrium models of adsorption, in: C.P. Bergmann, F.M. Machado (Eds.), Carbon Nanomaterials as Adsorbents for Environmental and Biological Applications, Springer International Publishing, Cham, 2015, pp. 33–69, https://doi.org/10.1007/978-3-319-18875-1_3.
[52] L.D.T. Prola, F.M. Machado, C.P. Bergmann, F.E. de Souza, C.R. Gally, E.C. Lima, M.A. Adebayo, S.L.P. Dias, T. Calvete, Adsorption of Direct Blue 53 dye from aqueous solutions by multi-walled carbon nanotubes and activated carbon, J. Environ. Manage. 130 (2013) 166–175, https://doi.org/10.1016/j.jenvman.2013.09.003.
[53] N. Khandelwal, E. Tiwari, N. Singh, R. Marsac, T. Schafer, F.A. Monikh, G. K. Darbha, Impact of long-term storage of various redox-sensitive supported nanocomposites on their application in removal of dyes from wastewater: Mechanisms delineation through spectroscopic investigations, J. Hazard. Mater. 401 (2021), 123375, https://doi.org/10.1016/j.jhazmat.2020.123375.
[54] H.K. Boparai, M. Joseph, D.M. O'Carroll, Cadmium (Cd2+) removal by nano zerovalent iron: surface analysis, effects of solution chemistry and surface complexation modeling, Environ. Sci. Pollut. Res. 20 (9) (2013) 6210–6221, https://doi.org/10.1007/s11356-013-1651-8.
[55] N. Ayawei, A.N. Ebelegi, D. Wankasi, Modeling and Interpretation of Adsorption Isotherms, J. Chem. 2017 (2017) 3039817, https://doi.org/10.1155/2017/3039817.
[56] S.-Y. Woo, H.-S. Lee, J.-S. Kim, K.-H. Kim, H. Ji, Y.-D. Kim, Applicability assessment of functional adsorption zeolite materials in adsorption desalination cum cooling systems driven by low-grade heat source, Chem. Eng. J. 430 (2022), 131375, https://doi.org/10.1016/j.cej.2021.131375.
[57] S. Raghav, D. Kumar, Adsorption equilibrium, kinetics, and thermodynamic studies of fluoride adsorbed by tetrametallic oxide adsorbent, J. Chem. Eng. Data 63 (5) (2018) 1682–1697, https://doi.org/10.1021/acs.jced.8b00024.
[58] Y. Cantu, A. Remes, A. Reyna, D. Martinez, J. Villarreal, H. Ramos, S. Trevino, C. Tamez, A. Martinez, T. Eubanks, J.G. Parsons, Thermodynamics, kinetics, and activation energy studies of the sorption of chromium(III) and chromium(VI) to a Mn_3O_4 nanomaterial, Chem Eng J 254 (2014) 374–383, https://doi.org/10.1016/j.cej.2014.05.110.

Supplementary Information

Varying growth behavior of redox-sensitive nanoparticles on 1:1 and 2:1 clay surfaces: mechanistic insights on preferential toxic ions removal in mono, co and multi-metal contaminated waters

Nitin Khandelwal[a,b], Nisha Singh[a,c], Ekta Tiwari[a,d], Rémi Marsac[e], Dieter Schild[f], Thorsten Schäfer[g], and Gopala Krishna Darbha[a,h,*]

[a]Environmental Nanoscience Laboratory, Department of Earth Sciences, Indian Institute of Science Education and Research (IISER) Kolkata, Mohanpur, West Bengal 741246, India

[b]Environmental Engineering Laboratory, Department of Civil Engineering, McGill University, Montreal H3A 0C3, Quebec, Canada

[c]Japan Agency for Marine-Earth Science and Technology (JAMSTEC), 2-15 Natsushima, Yokosuka, Kanagawa, 237-0061, Japan

[d]Natural Resources Management & Environmental Sciences, College of Agriculture, Food & Environmental Sciences, California Polytechnic State University, CA, 93401, USA

[e]Univ Rennes, CNRS, Géosciences Rennes - UMR 6118, F-35000 Rennes, France.

[f]Karlsruhe Institute of Technology (KIT), Institute for Nuclear Waste Disposal, Hermann-von-Helmholtz-Platz 1, 76344, Eggenstein-Leopoldshafen, Germany

[g]Institute of Geosciences, Applied Geology, Friedrich-Schiller-University Jena, Burgweg 11, D-07749, Jena, Germany

[h]Centre for Climate and Environmental Studies, Indian Institute of Science Education and Research (IISER) Kolkata, Mohanpur, West Bengal 741246, India

[*]Corresponding author: Gopala Krishna Darbha, Email- gkdarbha@gmail.com, gkdarbha80@yahoo.com Tel: (+91)- 9849626082

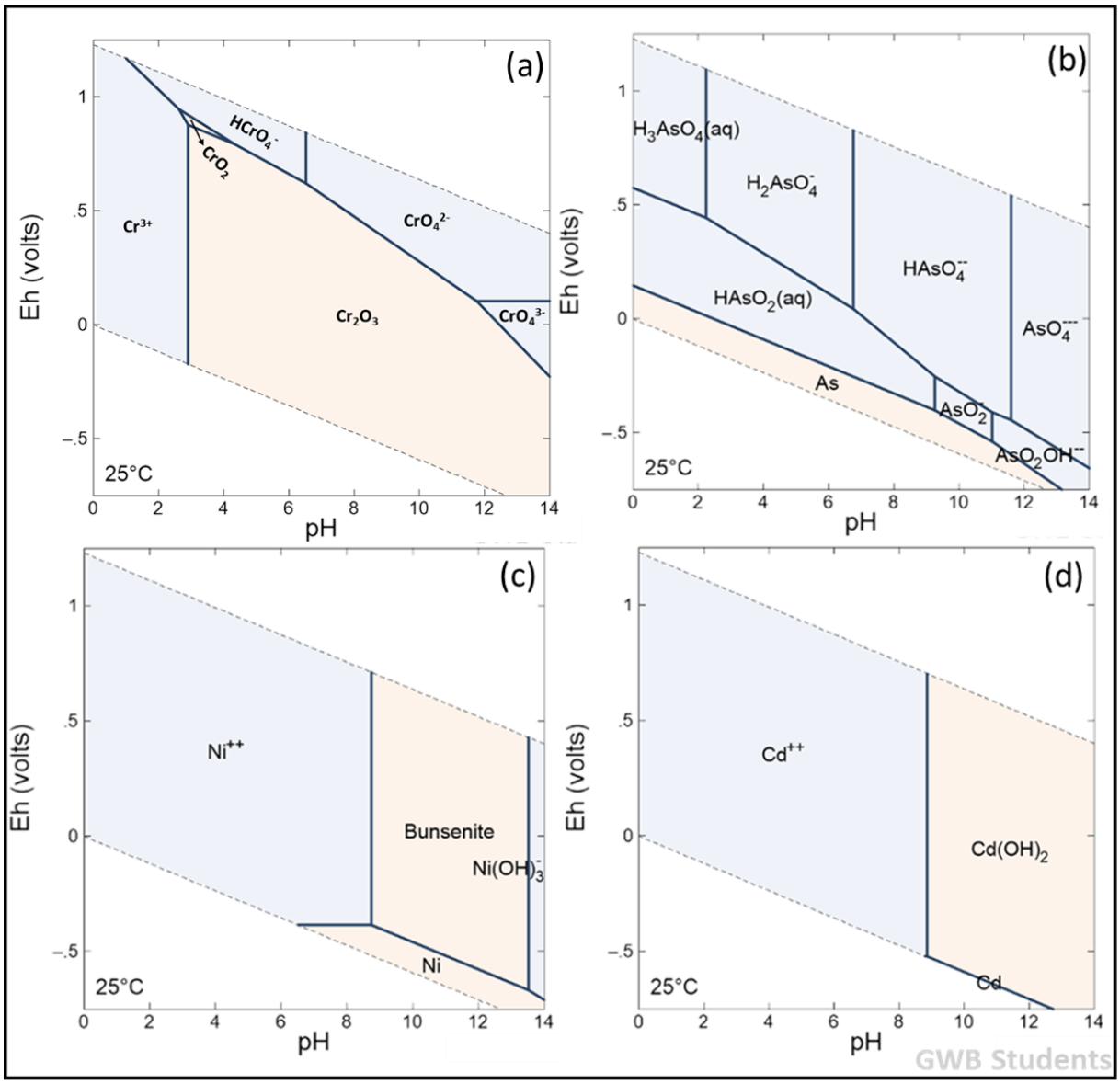

Fig. S1 Eh-pH speciation diagrams for (a) CrO_4^{2-}, (b) AsO_2^-, (c) Ni^{2+} and (d) Cd^{2+} [T= 25^0C, C= 1mM in presence of 0.01M $NaNO_3$]

Table S1 (a) Water compositions for SFW, SGW and natural river water

Water type/ Parameters	**SFW [1]**	**SGW [2]**	**RW (Hooghly)**
Na^+	0.25 mM	12.43 mM	0.53
Ca^{2+}	0.265 mM	2.00 mM	0.46
Mg^{2+}	0.06 mM	-	0.22
K^+	0.025 mM	-	0.063
NO_3^-	0.031 mM	1.00 mM	0.032
Cl^-	0.28 mM	4.50 mM	0.71
SO_4^{2-}	0.115 mM	1.50 mM	0.21
PO_4^{3-}	-	0.05 mM	-
HCO_3^-	0.385 mM	2.00 mM	1.23
SiO_3^{2-}	-	0.89 mM	-
DOM	1 mg/L	5 mg/L	1.9 mg/L
pH	7.4	7.3	8.4

Table S1 (b) Composition of synthetic waste water [3]

Component	**Amount**
Sucrose	727.5 mg/L
Sodium acetate	227.5 mg/L
NH_4Cl	250 mg/L
$MgCl_2$	45 mg/L
$CaCl_2.2H_2O$	22.5 mg/L
$NaHCO_3$	454.5 mg/L
Na_2HPO_4	24.25 mg/L
KH_2PO_4	14.75 mg/L

Note- pH of the final solution was 7.3

Table S2 BET surface area, average pore diameter, and cumulative pore volume of clays and synthesized nanocomposites

Samples	S_{BET} (m^2/g)	Average pore diameter (Å)	Pore volume (cm^3/g)
Bentonite	24.52	40.79	0.071
Kaolinite	3.15	81.3	0.009
B-nZVI	31.15	43.58	0.084
K-nZVI	19.42	51.5	0.063

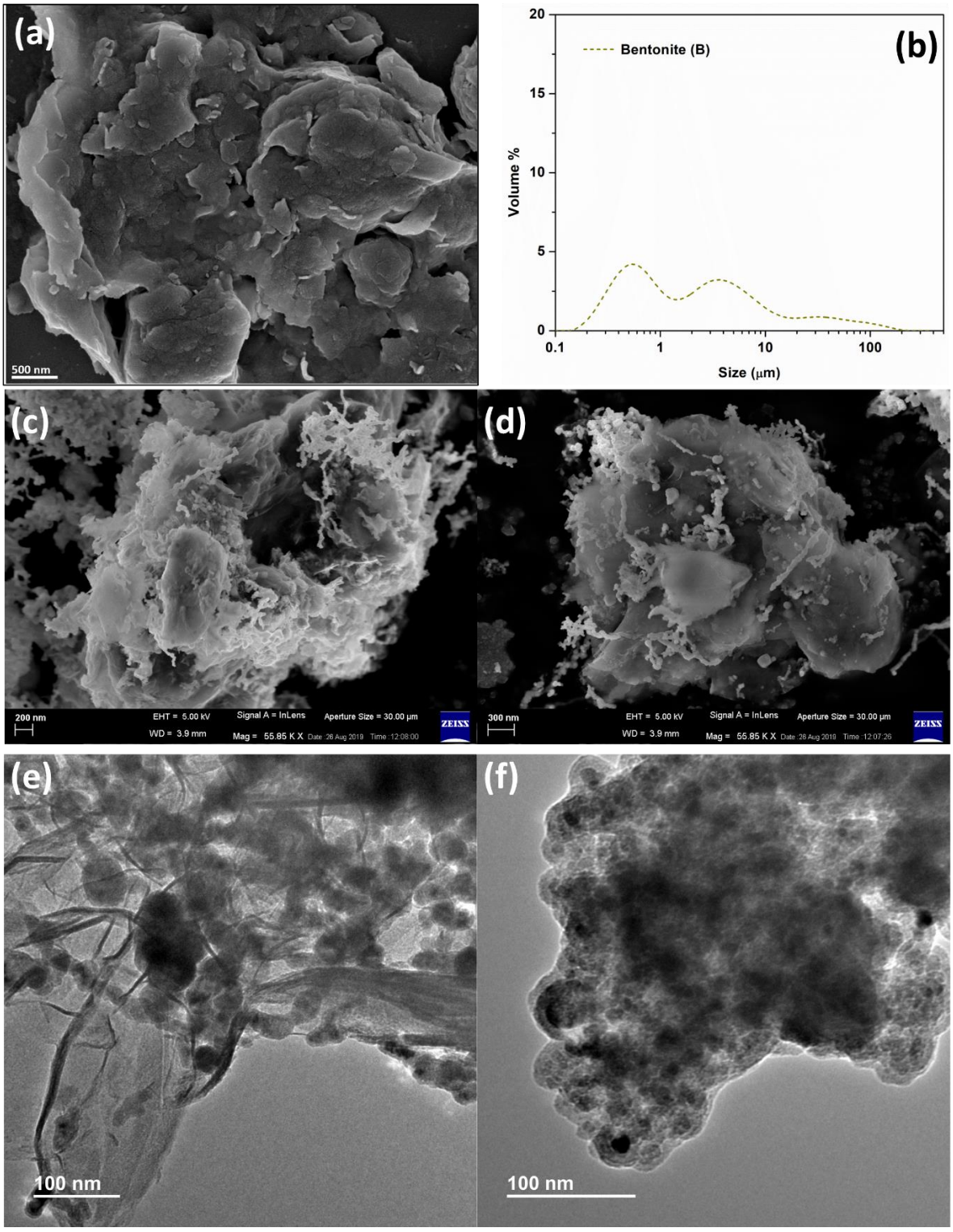

Fig. S2 (a) FESEM image and (b) particle size distribution of Bentonite, FESEM images (c-d) and TEM images (e-f) of B-nZVI composite

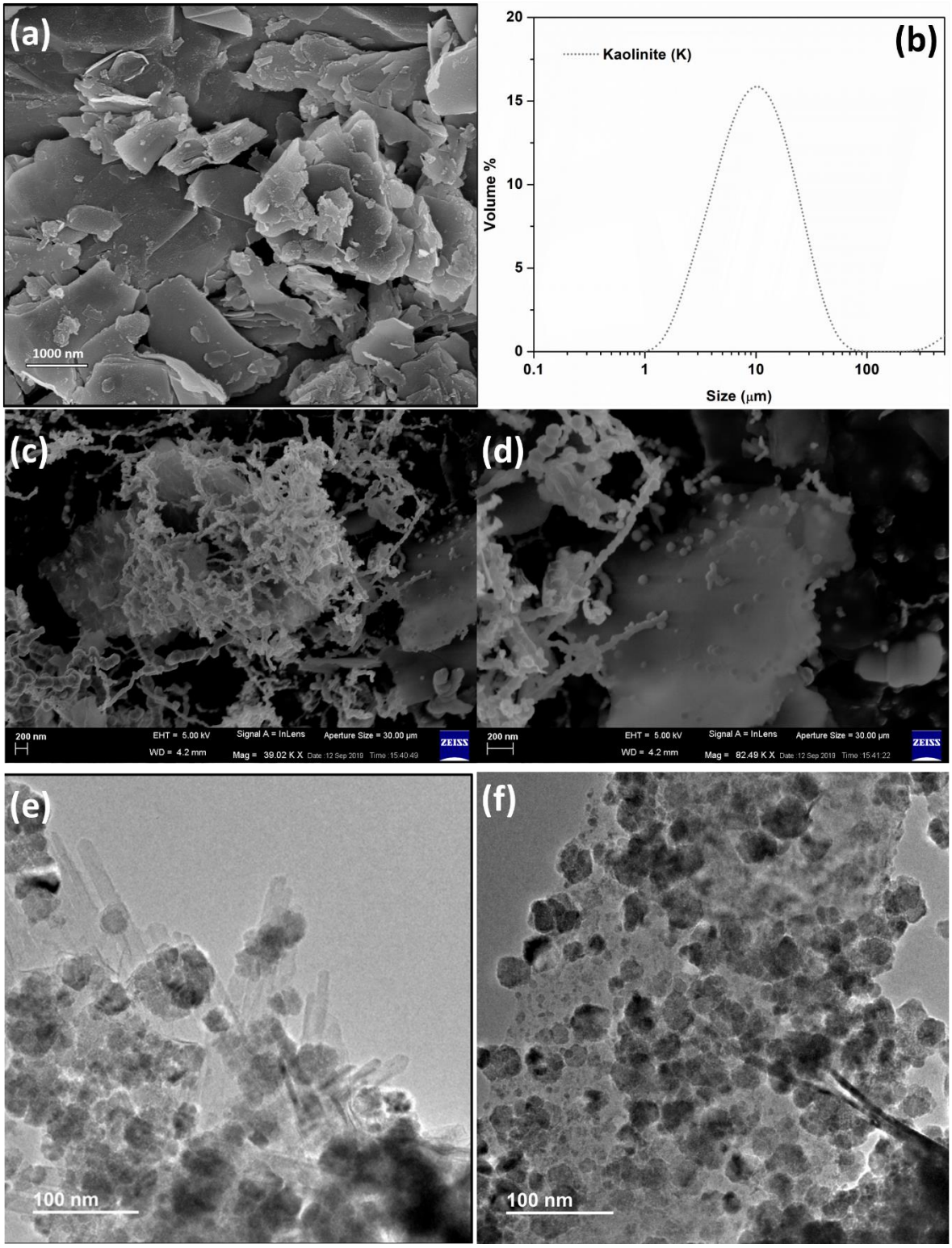

Fig. S3 (a) FESEM image and (b) particle size distribution of Kaolinite, FESEM images (c-d) and TEM images (e-f) of K-nZVI composite

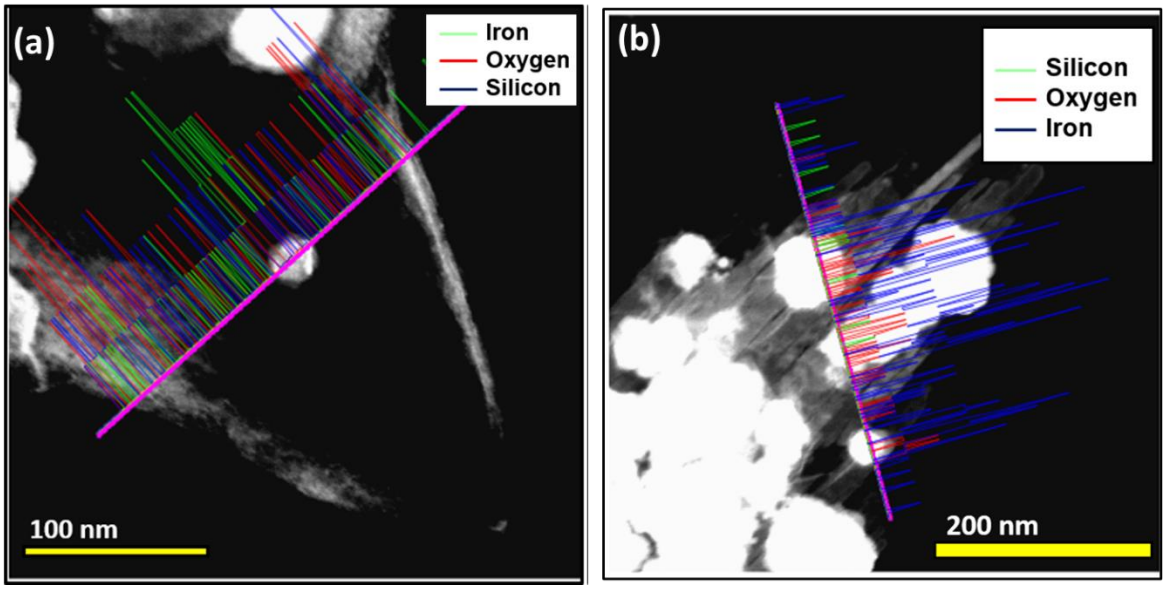

Fig. S4 Elemental line scan around nZVI particles in (a) B-nZVI and (b) K-nZVI

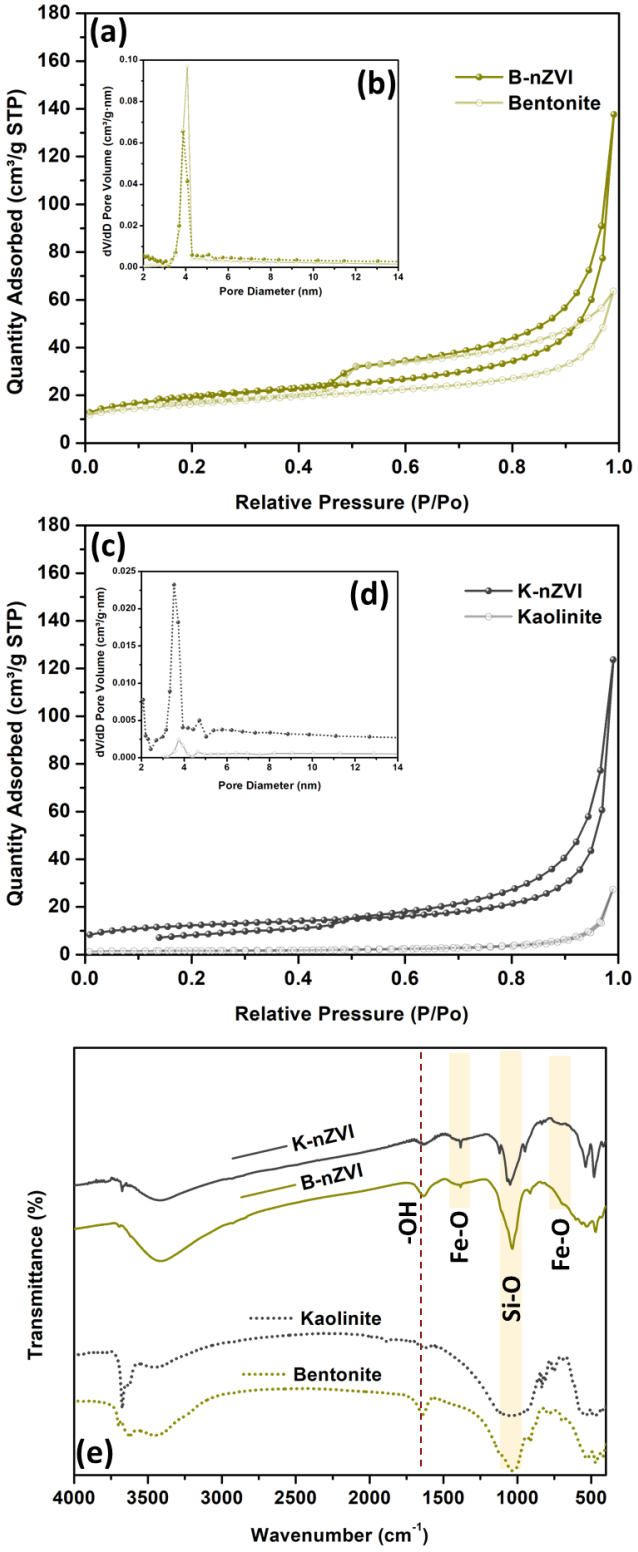

Fig. S5 (a-d) N_2 adsorption-desorption isotherm curve along with pore distribution (inset) curve for (a, b) Bentonite and B-nZVI and (c, d) Kaolinite and K-nZVI, and (e) FTIR spectra

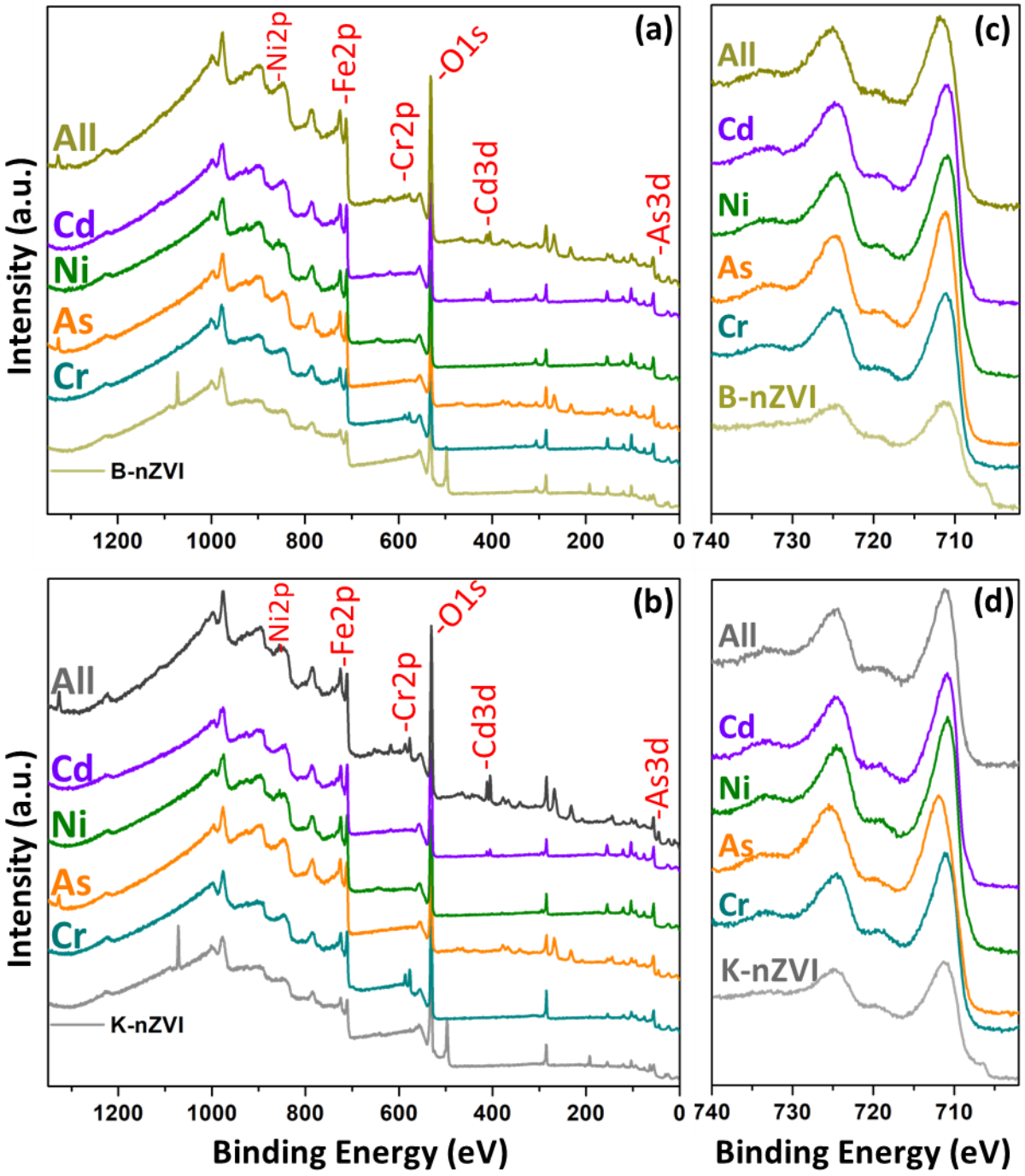

Fig. S6 XPS data for different composites and reaction precipitates showing (a, b) survey scans for reaction precipitates and (c, d) Fe2p region, before and after sorption experiments for B-nZVI and K-nZVI, respectively.

Section:1 Non-linear kinetics modelling

Kinetic models	Non-linear equations
pseudo-second-order	$q_t = q_e - \frac{q_e}{[k_2\,(q_e).\,t + 1]}$
General order	$q_t = q_e - \frac{q_e}{[k_N\,(q_e)^{n-1}.\,t.\,\,(n-1)+1]^{\frac{1}{1-n}}}$
Intra-particle diffusion (IPD)	$q_t = \,k_i\sqrt{t} + C$

Where:

q_e = Equilibrium sorption capacity (mg/g) , q_t = Sorption capacity at time= t (mg/g)

k_2 = second order reaction rate constant (g $mg^{-1}min^{-1}$), k_N = General order reaction rate constant [min^{-1} (g mg^{-1})$^{n-1}$] and k_i = intra particle diffusion rate constant (mg/g $hr^{0.5}$)

n= order of the reaction and intercept C gives resistance in mass transfer due to boundary layer

Pseudo 2nd order is with presumed order of two for the uptake of the contaminants i.e. pseudo 2nd order assumes that the rate of uptake of adsorbate is of 2nd order with respect to all the available sorption sites[4]. Logically, it would be better to obtain the order of a reaction kinetics from the experimental data itself rather than assuming any order. As the process of adsorption is considered to be the rate determining step, it helped in establishing the general order kinetic model. Which states that "the order of sorption process should follow the same trend as that of a chemical reaction, where the order of the reaction is not being restrained by a given model but experimentally" [5, 6]. Whereas, intra particle diffusion (IPD) is based on Fick's second law of diffusion [7].

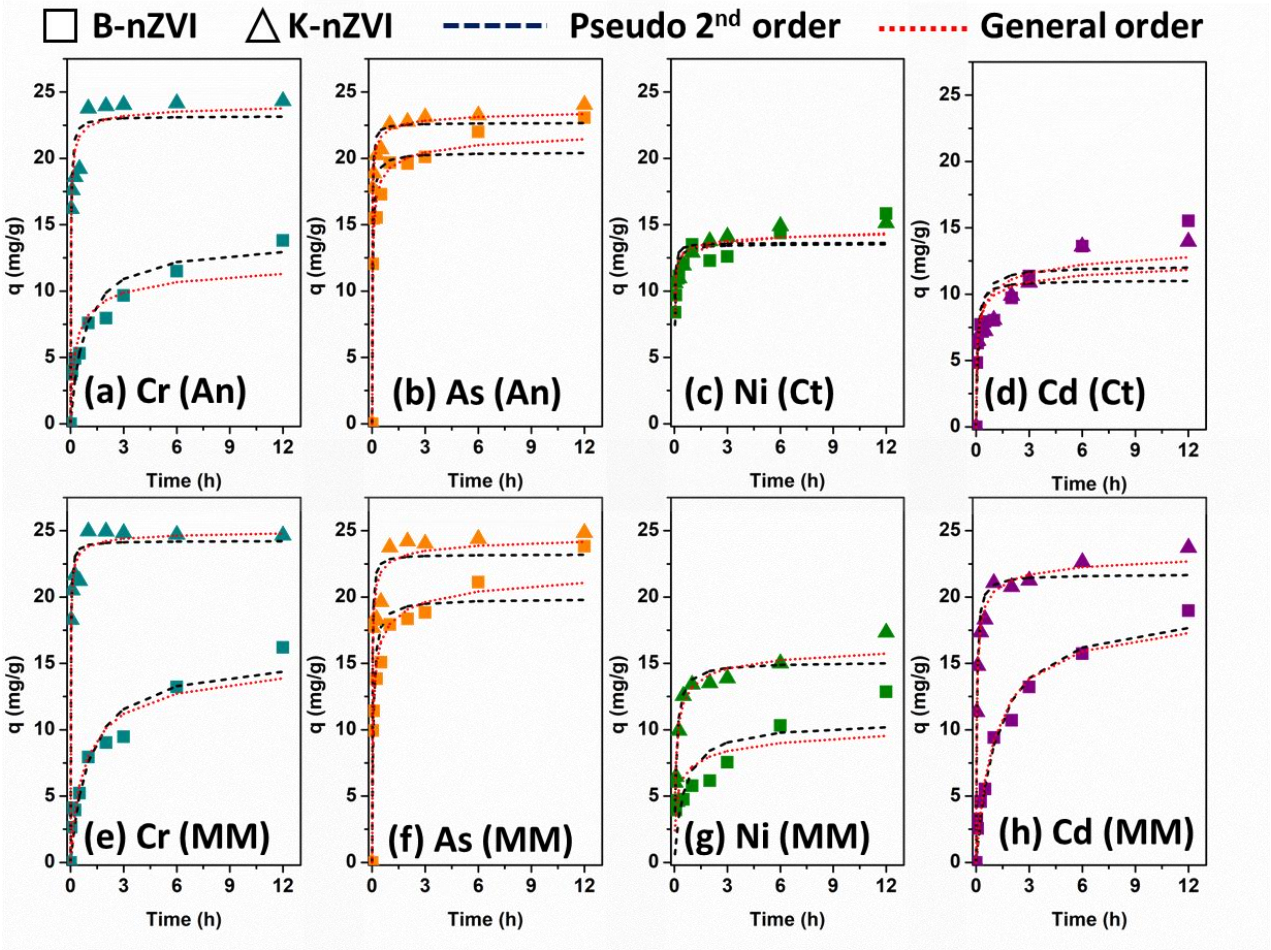

Fig. S5 Reaction kinetics modelling for B-nZVI and K-nZVI in (a-d) co-ionic and (e-h) multi-ionic contaminant systems [m= 20 mg, V= 20 mL, C_0= 20 mg/L, T= 25^{0}C, RPM= 200, pH= 6.5, t= 0-12h]

Table S3 (a) Obtained parameters from various kinetic models for B-nZVI and K-nZVI in mono-metallic species system

Kinetic models		Pseudo second order			General order				Intraparticle diffusion (IPD)		
Adsorbate		K_2 (g $mg^{-1}h^{-1}$)	q (mg/g)	R^2	K_n (h^{-1} (g $mg^{-1})^{n-1}$)	q (mg/g)	n	R^2	K (mg/g $h^{1/2}$)	Intercept	R^2
CrO_4^{2-}	B-nZVI	0.61	13.70	0.89	0.01	13.90	4.08	0.96	3.17	3.46	0.97
	K-nZVI	2.78	24.09	0.97	0.12	25.15	3.24	0.99	8.32	14.6	0.88
AsO_2^-	B-nZVI	0.98	23.24	0.96	0.15	23.85	2.70	0.97	13.1	10.41	0.96
	K-nZVI	3.89	25.10	1.00	4.38	25.06	1.95	1.00	16.4	16.6	0.99
Ni^{2+}	B-nZVI	2.45	16.24	0.90	0.01	18.62	4.34	0.96	3.22	10.94	0.95
	K-nZVI	2.79	11.21	0.94	0.08	12.33	3.69	0.98	4.35	6.28	0.98
Cd^{2+}	B-nZVI	7.39	16.76	0.98	0.02	18.34	4.82	0.99	1.42	14.37	0.92
	K-nZVI	3.86	12.05	0.89	0.001	14.27	4.91	0.95	2.33	8.29	0.83

Table S3 (b) Obtained parameters from various kinetic models for B-nZVI and K-nZVI in co-ionic metal species system

Kinetic models		Pseudo second order			General order				Intraparticle diffusion (IPD)		
Adsorbate		K_2 (g $mg^{-1}h^{-1}$)	q (mg/g)	R^2	K_n (h^{-1} (g $mg^{-1})^{n-1}$)	q (mg/g)	n	R^2	K (mg/g $h^{1/2}$)	Intercept	R^2
CrO_4^{2-}	B-nZVI	0.09	13.80	0.91	0.001	13.50	3.73	0.91	4.00	2.86	0.97
	K-nZVI	2.11	23.19	0.95	0.10	24.42	3.19	0.98	6.79	17.68	0.80
AsO_2^-	B-nZVI	1.66	20.45	0.94	0.001	23.18	4.07	0.99	13.1	6.2	0.88
	K-nZVI	3.73	22.68	0.98	0.07	24.08	3.64	0.98	5.51	17.07	0.95
Ni^{2+}	B-nZVI	2.70	13.55	0.94	0.01	15.84	4.54	0.97	5.96	7.75	0.96
	K-nZVI	5.07	13.64	0.93	0.03	15.18	4.35	0.98	2.04	10.38	0.93
Cd^{2+}	B-nZVI	0.69	12.12	0.80	0.001	15.63	4.86	0.92	2.89	5.9	0.96
	K-nZVI	1.44	11.05	0.74	0.001	14.20	5.16	0.88	3.2	5.4	0.97

Table S3 (c) Obtained parameters from various kinetic models for B-nZVI and K-nZVI in multi-ionic metal species system

Kinetic models		Pseudo second order			General order				Intraparticle diffusion (IPD)		
Adsorbate		K_2 (g $mg^{-1}h^{-1}$)	q (mg/g)	R^2	K_n (h^{-1} (g $mg^{-1})^{n-1}$)	q (mg/g)	n	R^2	K (mg/g $h^{1/2}$)	Intercept	R^2
CrO_4^{2-}	B-nZVI	0.06	15.64	0.92	0.001	16.79	3.00	0.92	4.17	4.66	0.71
	K-nZVI	3.24	24.24	0.98	0.25	25.21	3.01	0.99	7.44	16.8	0.97
AsO_2^-	B-nZVI	0.83	19.89	0.90	0.001	23.92	4.36	0.96	9.45	8.57	0.98
	K-nZVI	2.52	23.22	0.93	0.03	25.13	3.62	0.97	6.94	15.81	0.80
Ni^{2+}	B-nZVI	0.18	10.64	0.73	0.001	13.17	6.01	0.76	2.91	2.74	0.95
	K-nZVI	0.91	15.13	0.95	0.01	17.36	3.62	0.97	1.63	11.35	0.97
Cd^{2+}	B-nZVI	0.04	19.44	0.97	0.03	19.25	2.19	0.96	3.93	5.68	0.97
	K-nZVI	2.17	21.72	0.97	0.01	24.07	3.54	0.99	8.42	12.63	0.97

Section-2: Adsorption Isotherm models

Isotherm models	Non-linear equations
Langmuir	$q_e = \frac{q_m K_L C_e}{1 + K_L C_e}$
Freundlich	$q_e = K_F C_e^n$
Sip	$q = q_{max} \frac{K[C_e]^n}{1 + K[C_e]^n}$

Where:

C_e (mg/L) = equilibrium concentration,

q_e = sorption capacity at equilibrium (mg/g),

q_m = obtained maximum sorption capacity (mg/g) and

K_L = Langmuir constants (L/mg) related to energy of adsorption

K_F = Freundlich adsorption constant (mg/g)(L/mg)$^{1/n}$ and

n = a measure of the adsorption intensity (Freundlich)

K = Sips isotherm constant

n = Sips isotherm exponent

Isotherm is generally utilized to evaluate interactions between adsorbate and adsorbent. Commonly used isotherms include Langmuir model which assumes monolayer sorption of the adsorbate on adsorbent surface. It suggests that all the sorption sites are identical and energetically equivalent [8, 9]. Freundlich model assumes heterogeneous nature of the surface and represents initial sorption on surface followed by condensation effect causing strong adsorbate-adsorbent interaction. To depict isotherm data better, Sip's isotherm model can be used. This model is a combination of both Langmuir and Freundlich model. At low adsorbate concentration this model predicts Freundlich like behavior which converts to plateau or monolayer sorption at higher concentrations [10].

Table S4 (a) Obtained parameters from various isotherm models for B-nZVI and K-nZVI in mono-metallic species system

Sorption isotherm models		Langmuir			Freundlich			Sips			
Adsorbate		q_{max} (mg/g)	K_L	R^2	K_f	n	R^2	q_{max} (mg/g)	K	n	R^2
CrO_4^{2-}	B-NZVI	19.96	0.26	0.81	10.20	0.16	0.69	18.44	0.05	1.85	0.85
	K-NZVI	38.90	24.71	0.71	31.21	0.09	0.88	87.47	0.57	0.14	0.87
AsO_2^-	B-NZVI	41.22	1.01	0.91	23.29	0.18	1.00	86.88	0.36	0.30	1.00
	K-NZVI	57.45	7.51	0.90	42.17	0.17	0.96	157.35	0.37	0.24	0.96
Ni^{2+}	B-NZVI	38.02	0.18	0.99	12.38	0.28	0.95	36.00	0.15	1.18	0.99
	K-NZVI	36.24	0.07	0.86	6.27	0.40	0.79	25.09	0.08	1.36	0.95
Cd^{2+}	B-NZVI	44.77	0.12	0.93	10.46	0.36	0.90	46.06	0.13	0.95	0.93
	K-NZVI	20.99	0.22	0.66	9.23	0.20	0.68	27.09	0.35	0.52	0.68

Table S4 (b) Obtained parameters from various isotherm models for B-nZVI and K-nZVI in co-ionic metal species system

Sorption isotherm models		Langmuir			Freundlich			Sips			
Adsorbate		q_{max} (mg/g)	K_L	R^2	K_f	n	R^2	q_{max} (mg/g)	K	n	R^2
CrO_4^{2-}	B-NZVI	31.40	0.08	0.98	5.89	0.39	0.99	51.07	0.09	0.61	0.99
	K-NZVI	46.41	1.67	0.97	27.80	0.19	1.00	126.93	0.28	0.26	1.00
AsO_2^-	B-NZVI	39.47	0.79	0.98	21.47	0.19	0.99	98.23	0.27	0.28	0.99
	K-NZVI	46.40	1.04	0.94	23.72	0.24	0.99	121.36	0.24	0.33	0.99
Ni^{2+}	B-NZVI	35.64	0.10	0.99	8.06	0.35	0.99	37.28	0.11	0.92	0.99
	K-NZVI	20.95	0.25	1.00	10.21	0.17	0.99	19.56	0.09	1.57	1.00
Cd^{2+}	B-NZVI	29.08	0.13	0.99	8.34	0.30	1.00	26.09	0.10	1.27	0.99
	K-NZVI	13.32	235.05	0.99	13.31	0.00	0.99	13.32	0.10	1.27	0.86

Table S4 (c) Obtained parameters from various isotherm models for B-nZVI and K-nZVI in multi-ionic metal species system

Sorption isotherm models		Langmuir			Freundlich			Sips			
Adsorbate		q_{max} (mg/g)	K_L	R^2	K_f	n	R^2	q_{max} (mg/g)	K	n	R^2
CrO_4^{2-}	B-NZVI	36.42	0.09	0.97	6.93	0.40	0.99	62.17	0.10	0.60	0.98
	K-NZVI	42.70	5.81	0.99	33.06	0.09	0.96	98.09	0.51	0.14	0.96
AsO_2^-	B-NZVI	58.36	0.48	0.94	21.85	0.34	0.99	131.57	0.20	0.46	0.98
	K-NZVI	51.77	5.26	0.93	35.77	0.18	1.00	169.63	0.27	0.24	1.00
Ni^{2+}	B-NZVI	16.66	0.34	0.99	9.49	0.13	0.99	20.09	0.62	0.46	0.99
	K-NZVI	17.66	12.18	0.99	17.31	0.00	0.99	17.63	0.06	3.76	0.99
Cd^{2+}	B-NZVI	109.30	0.03	0.97	5.51	0.68	0.98	113.18	0.04	0.91	0.97
	K-NZVI	51.54	0.61	0.97	22.98	0.27	1.00	87.09	0.34	0.46	1.00

Table S5 ΔG values for removal of chromium, arsenic, nickel and cadmium using B-nZVI and K-nZVI in mono, co, and multi-ionic contaminated solutions

Mono-ionic contamination		**Co-ionic contamination**		**Multi-ionic contamination**	
B-nZVI	**ΔG (KJ/mol)**	**B-nZVI**	**ΔG (KJ/mol)**	**B-nZVI**	**ΔG (KJ/mol)**
Cr	-19.5	**Cr**	-20.9	**Cr**	-21.2
As	-25.3	**As**	-24.6	**As**	-23.8
Ni	-22.5	**Ni**	-21.7	**Ni**	-26.0
Cd	-23.8	**Cd**	-23.1	**Cd**	-20.8
K-nZVI	**ΔG (KJ/mol)**	**K-nZVI**	**ΔG (KJ/mol)**	**K-nZVI**	**ΔG (KJ/mol)**
Cr	-25.5	**Cr**	-23.8	**Cr**	-21.2
As	-25.4	**As**	-24.3	**As**	-24.6
Ni	-20.6	**Ni**	-21.2	**Ni**	-20.2
Cd	-26.2	**Cd**	-23.1	**Cd**	-26.1

Table S6 Summary of reported adsorbents and their contaminants sorption capacities

Adsorbents	Sorption capacity (mg/g)				Reference
	Ni	Cr	As	Cd	
Bentonite-nZVI *Mono-ionic*	36	18.4	86.8	46.1	**This study**
Kaolinite-nZVI *Mono-ionic*	25.1	87.4	157.3	27.1	**This study**
Bentonite-nZVI *Co-ionic*	37.3	51.1	98.2	26.1	**This study**
Kaolinite-nZVI *Co-ionic*	19.6	126.9	121.3	13.3	**This study**
Bentonite-nZVI *Multi-ionic*	20.1	62.2	131.6	113.2	**This study**
Kaolinite-nZVI *Multi-ionic*	17.7	98.1	169.6	87.1	**This study**
Bentonite supported nZVI	50.25	9			[11, 12]
Bentonite-nZVI	16.5			14.25	[12]
Activated alumina		25.57			[13]
Nano- alumina	30.82	-			[14]
(nZVI)-Fe_3O_4 nanocomposites		20.41			[15]
Biochar-nZVI	47.85	23.09	-	39.53	[16]
coal fly ash-nZVI				200	[17]
Magnetic magnetite (Fe_3O_4)		20.16			[18]
Biochar-magnetite			5.49		[19]

Ascorbic acid coated Fe3O4 nanoparticles			46.06		[20]
Modified activated carbon	78.12	-			[21]
Au-nZVI				40- 188	[22]
Activated carbon (AC)		9.89			[23]
AC-nZVI		25	18.2		[23, 24]
Nanoscale Fe-Mn Binary Oxides Loaded on Zeolite			296.23		[25]

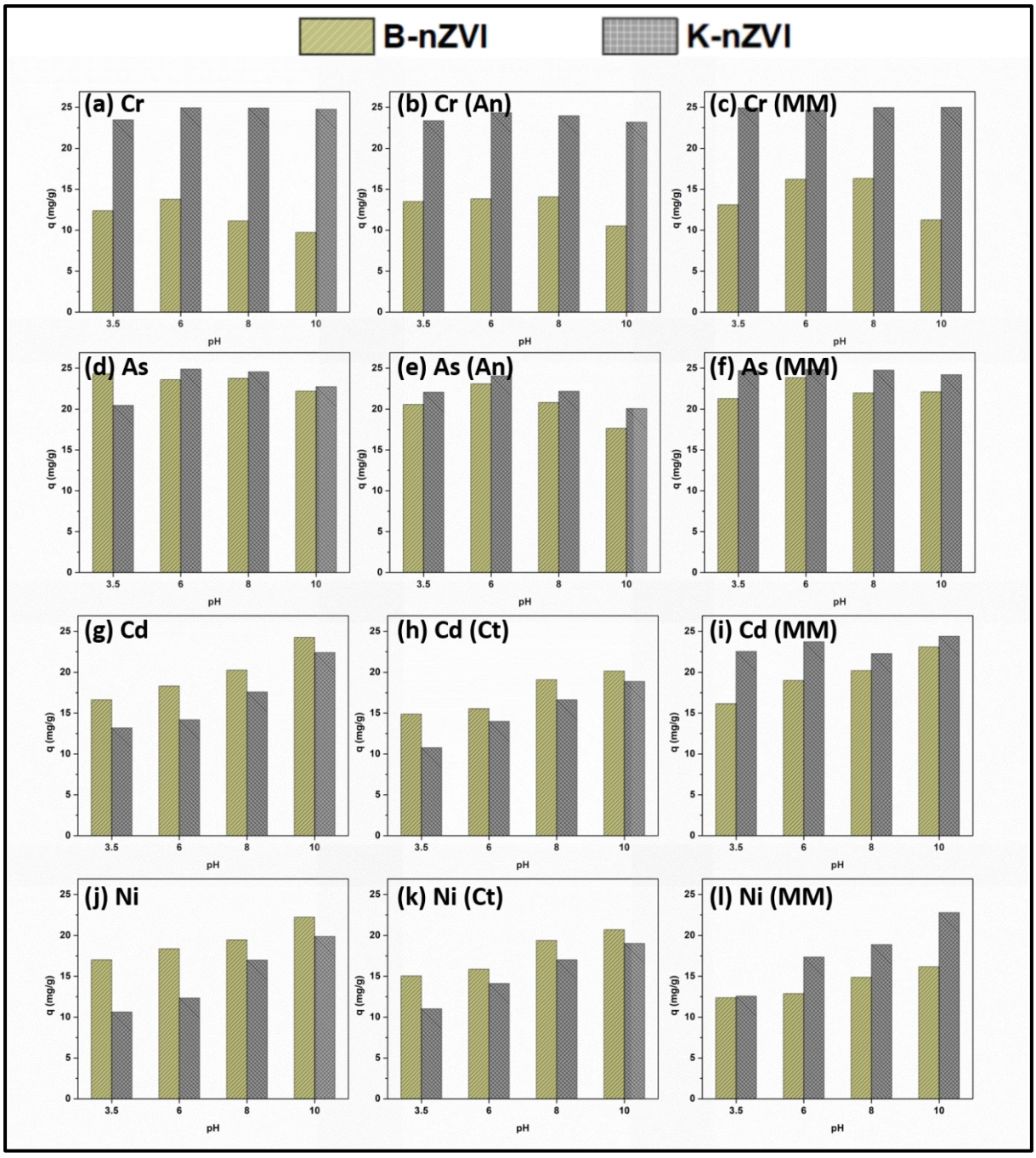

Fig. S6 (a-l) Effect of solution pH on sorption capacities of B-nZVI and K-nZVI in mono-ionic, co-ionic and multi-ionic metal species system [m= 20 mg, V= 20 mL, C_0= 20 mg/L, T= 25^0C, RPM= 200, t= 12h]

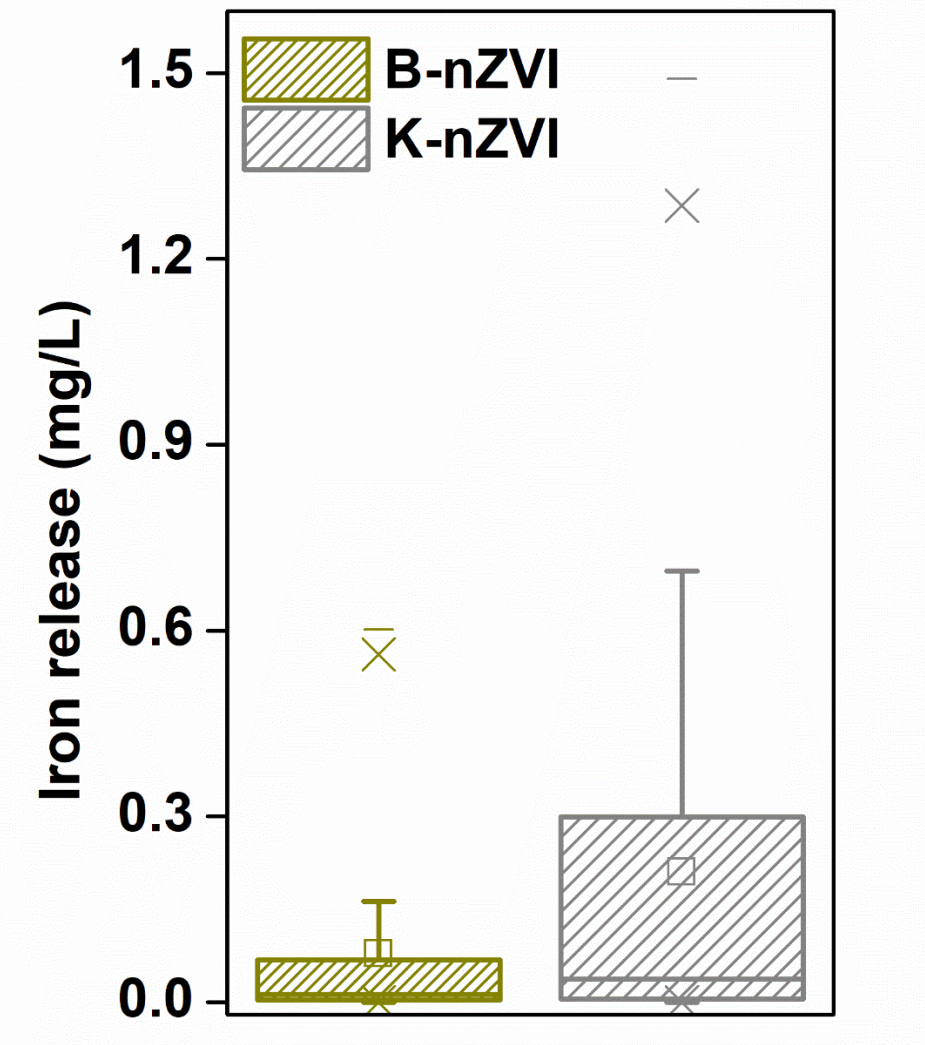

Fig. S7 Iron release from the composites in performed sorption experiments

References

[1] E.J. Smith, W. Davison, J. Hamilton-Taylor, Methods for preparing synthetic freshwaters, Water Res 36(5) (2002) 1286-1296. https://doi.org/Pii S0043-1354(01)00341-4

Doi 10.1016/S0043-1354(01)00341-4.

[2] H. Xu, Y. Sun, J. Li, F. Li, X. Guan, Aging of Zerovalent Iron in Synthetic Groundwater: X-ray Photoelectron Spectroscopy Depth Profiling Characterization and Depassivation with Uniform Magnetic Field, Environ Sci Technol 50(15) (2016) 8214-8222. https://doi.org/10.1021/acs.est.6b01763.

[3] W. Cherdchoo, S. Nithettham, J. Charoenpanich, Removal of Cr(VI) from synthetic wastewater by adsorption onto coffee ground and mixed waste tea, Chemosphere 221 (2019) 758-767. https://doi.org/10.1016/j.chemosphere.2019.01.100.

[4] Y.S. Ho, G. McKay, Pseudo-second order model for sorption processes, Process Biochem 34(5) (1999) 451-465. https://doi.org/Doi 10.1016/S0032-9592(98)00112-5.

[5] A.G.N. Wamba, E.C. Lima, S.K. Ndi, P.S. Thue, J.G. Kayem, F.S. Rodembusch, G.S. dos Reis, W.S. de Alencar, Synthesis of grafted natural pozzolan with 3-aminopropyltriethoxysilane: preparation, characterization, and application for removal of Brilliant Green 1 and Reactive Black 5 from aqueous solutions, Environ Sci Pollut R 24(27) (2017) 21807-21820. https://doi.org/10.1007/s11356-017-9825-4.

[6] Y. Liu, L. Shen, A general rate law equation for biosorption, Biochem Eng J 38(3) (2008) 390-394. https://doi.org/https://doi.org/10.1016/j.bej.2007.08.003.

[7] J.-P. Simonin, J. Bouté, Intraparticle diffusion-adsorption model to describe liquid/solid adsorption kinetics, Revista Mexicana De Ingenieria Quimica 15(1) (2016) 161-173.

[8] H.K. Boparai, M. Joseph, D.M. O'Carroll, Kinetics and thermodynamics of cadmium ion removal by adsorption onto nano zerovalent iron particles, J Hazard Mater 186(1) (2011) 458-465. https://doi.org/10.1016/j.jhazmat.2010.11.029.

[9] N. Ayawei, A.N. Ebelegi, D. Wankasi, Modelling and Interpretation of Adsorption Isotherms, J Chem-Ny (2017). https://doi.org/Artn 3039817

10.1155/2017/3039817.

[10] A. Nimibofa, A. Ebelegi, W. Donbebe, Modelling and Interpretation of Adsorption Isotherms, Hindawi Journal of Chemistry Volume 2017 (2017) 11 pages. https://doi.org/10.1155/2017/3039817.

[11] L.N. Shi, X. Zhang, Z.L. Chen, Removal of Chromium (VI) from wastewater using bentonite-supported nanoscale zero-valent iron, Water Res 45(2) (2011) 886-892. https://doi.org/10.1016/j.watres.2010.09.025.

[12] N.A. Zarime, W.Z.W. Yaacob, H. Jamil, Removal of heavy metals using bentonite supported nano-zero valent iron particles, AIP Conference Proceedings 1940(1) (2018) 020029. https://doi.org/10.1063/1.5027944.

[13] A.K. Bhattacharya, T.K. Naiya, S.N. Mandal, S.K. Das, Adsorption, kinetics and equilibrium studies on removal of Cr(VI) from aqueous solutions using different low-cost adsorbents, Chem Eng J 137(3) (2008) 529-541. https://doi.org/https://doi.org/10.1016/j.cej.2007.05.021.

[14] V. Srivastava, C.H. Weng, V.K. Singh, Y.C. Sharma, Adsorption of Nickel Ions from Aqueous Solutions by Nano Alumina: Kinetic, Mass Transfer, and Equilibrium Studies, Journal of Chemical & Engineering Data 56(4) (2011) 1414-1422. https://doi.org/10.1021/je101152b.

[15] X.S. Lv, Y.J. Hu, J. Tang, T.T. Sheng, G.M. Jiang, X.H. Xu, Effects of co-existing ions and natural organic matter on removal of chromium (VI) from aqueous solution by nanoscale zero valent iron (nZVI)-Fe3O4 nanocomposites, Chem Eng J 218 (2013) 55-64. https://doi.org/10.1016/j.cej.2012.12.026.

[16] S.S. Zhu, S.H. Ho, X.C. Huang, D.W. Wang, F. Yang, L. Wang, C.Y. Wang, X.D. Cao, F. Ma, Magnetic Nanoscale Zerovalent Iron Assisted Biochar: Interfacial Chemical Behaviors and Heavy Metals Remediation Performance, Acs Sustain Chem Eng 5(11) (2017) 9673-9682. https://doi.org/10.1021/acssuschemeng.7b00542.

[17] L. Ma, Q. Wei, Y. Chen, Q. Song, C. Sun, Z. Wang, G. Wu, Removal of cadmium from aqueous solutions using industrial coal fly ash-nZVI, Roy Soc Open Sci 5(2) (2018) 171051-171051. https://doi.org/10.1098/rsos.171051.
[18] S. Rajput, C.U. Pittman, Jr., D. Mohan, Magnetic magnetite (Fe3O4) nanoparticle synthesis and applications for lead (Pb2+) and chromium (Cr6+) removal from water, J Colloid Interface Sci 468 (2016) 334-346. https://doi.org/10.1016/j.jcis.2015.12.008.
[19] C.M. Navarathna, A.G. Karunanayake, S.R. Gunatilake, C.U. Pittman, F. Perez, D. Mohan, T. Mlsna, Removal of Arsenic(III) from water using magnetite precipitated onto Douglas fir biochar, J Environ Manage 250 (2019) 109429. https://doi.org/https://doi.org/10.1016/j.jenvman.2019.109429.
[20] L. Feng, M. Cao, X. Ma, Y. Zhu, C. Hu, Superparamagnetic high-surface-area Fe3O4 nanoparticles as adsorbents for arsenic removal, J Hazard Mater 217-218 (2012) 439-446. https://doi.org/https://doi.org/10.1016/j.jhazmat.2012.03.073.
[21] M.O. Abd El-Magied, A.M.A. Hassan, H.M.H. Gad, T.F. Mohammaden, M.A.M. Youssef, Removal of nickel (II) ions from aqueous solutions using modified activated carbon: A kinetic and equilibrium study, Journal of Dispersion Science and Technology 39(6) (2018) 862-873. https://doi.org/10.1080/01932691.2017.1402337.
[22] Y. Su, A.S. Adeleye, Y. Huang, X. Sun, C. Dai, X. Zhou, Y. Zhang, A.A. Keller, Simultaneous removal of cadmium and nitrate in aqueous media by nanoscale zerovalent iron (nZVI) and Au doped nZVI particles, Water Res 63 (2014) 102-111. https://doi.org/https://doi.org/10.1016/j.watres.2014.06.008.
[23] S. Mortazavian, H. An, D. Chun, J. Moon, Activated carbon impregnated by zero-valent iron nanoparticles (AC/nZVI) optimized for simultaneous adsorption and reduction of aqueous hexavalent chromium: Material characterizations and kinetic studies, Chem Eng J 353 (2018) 781-795. https://doi.org/10.1016/j.cej.2018.07.170.
[24] H. Zhu, Y. Jia, X. Wu, H. Wang, Removal of arsenic from water by supported nano zero-valent iron on activated carbon, J Hazard Mater 172(2) (2009) 1591-1596. https://doi.org/https://doi.org/10.1016/j.jhazmat.2009.08.031.
[25] S. Kong, Y. Wang, Q. Hu, A.K. Olusegun, Magnetic nanoscale Fe–Mn binary oxides loaded zeolite for arsenic removal from synthetic groundwater, Colloids and Surfaces A: Physicochemical and Engineering Aspects 457 (2014) 220-227. https://doi.org/https://doi.org/10.1016/j.colsurfa.2014.05.066.